

Structure of Saturn's Mesosphere from the 28 Sgr Occultations

W. B. Hubbard,^{1,2} C. C. Porco,^{1,2} D. M. Hunten,¹ G. H. Rieke,^{1,3} M. J. Rieke,³ D. W. McCarthy,³ V. Haemmerle,¹
J. Haller,³ B. McLeod,³ L. A. Lebofsky,¹ R. Marcialis,¹ and J. B. Holberg¹

University of Arizona, Tucson, Arizona 85721
E-mail: hubbard@lpl.arizona.edu

R. Landau and L. Carrasco⁴

Observatorio Astronómico Nacional de San Pedro Mártir, 22860 Ensenada, Baja California, Mexico

J. Elias⁵

Cerro Tololo Inter-American Observatory, National Optical Astronomy Observatories, La Serena, Chile 1353

M. W. Buie and E. W. Dunham

Lowell Observatory, Flagstaff, Arizona 86001

S. E. Persson, T. Boroson,⁵ and S. West³

Carnegie Observatories, 813 Santa Barbara St., Pasadena, California 91101

R. G. French

Astronomy Department, Wellesley College, Wellesley, Massachusetts 02181

J. Harrington⁶ and J. L. Elliot

Department of Earth, Atmospheric, and Planetary Sciences, Massachusetts Institute of Technology, Cambridge, Massachusetts 02139

W. J. Forrest and J. L. Pipher

University of Rochester, Rochester, New York 14627

R. J. Stover

UCO/Lick Observatory, University of California, Santa Cruz, California 95064

and

A. Brahic and I. Grenier

Université Paris VII Denis Diderot, Observatoire de Paris, 92190 Meudon, France

Received March 21, 1997; revised September 9, 1997

¹ Lunar and Planetary Laboratory.

² Visiting Astronomer, Cerro Tololo Inter-American Observatory, National Optical Astronomy Observatories, operated by the Association of Universities for Research in Astronomy, Inc., under cooperative agreement with the National Science Foundation.

³ Steward Observatory.

⁴ Present address: INAOE, P.O. Box 51, Puebla, Pue., México.

⁵ Present address: NOAO, P.O. Box 26732, Tucson AZ 85726.

⁶ Present address: Goddard Space Flight Center, Code 693, Greenbelt, Maryland 20771

We analyze an extensive data set of immersion and emersion lightcurves of the occultation of 28 Sgr by Saturn's atmosphere on 3 July 1989. The data give profiles of number density as a function of altitude at a variety of latitudes, at pressures ranging from about 0.5 to about 20 μ bar. The atmosphere is essentially isothermal in this range, with a temperature close to 140 K for an assumed mean molecular weight of 2.135. Owing to favorable ring geometry, an accurate radial scale is available for all observations, and we confirm the substantial equatorial bulge pro-

duced by zonal winds of ~ 450 m/s first observed in the Voyager radio-occultation experiments. The fact that the bulge is still present at microbar pressures suggests that the equatorial winds persist to high altitudes. According to our radial scale, the $2.4\text{-}\mu\text{bar}$ level, which corresponds to half-flux in the stellar occultations, is at an equatorial radius of $60,960$ km. This radial scale is in good agreement with the Voyager radio-occultation data at mbar pressures and allows smooth interpolation of the isothermal structure between the stellar-occultation and radio-occultation regions. We do not have such a smooth interpolation between our data and Voyager ultraviolet occultation data, unless we discard the lowest 200 km of Voyager ultraviolet data. When this is done, we obtain a complete atmospheric model from an equatorial radius of $61,500$ km down to an equatorial radius of $60,500$ km. This model gives excellent agreement between all 28 Sgr, Voyager, and Pioneer 11 data.

© 1997 Academic Press

Key Words: occultations; Saturn, atmosphere; Saturn.

1. INTRODUCTION

Multiple observations of the 3 July 1989 occultation of the bright star 28 Sgr by Saturn's atmosphere, ring system, and satellite Titan (Nicholson, McGhee, and French 1995, French *et al.* 1993, Hubbard *et al.* 1993a, Sicardy *et al.* 1990, Hubbard *et al.* 1993b, Harrington *et al.* 1993) provide a rich source of ground-based information about the Saturn system at a level of precision comparable to that of spacecraft data. The present paper reports further analysis of this remarkable data set, leading to a synthesis of all major data records of the immersion and emersion of 28 Sgr in Saturn's atmosphere. We present a self-consistent global model of the structure and shape of the portions of the atmosphere probed by the star, analogous to the model of Titan's atmosphere derived by Hubbard *et al.* (1993b). We also place this model in the context of available spacecraft data, as was done for Jupiter by Hubbard *et al.* (1995).

When a bright star is occulted by a giant planet's atmosphere, normally the solution for the projected star position with respect to the position of the planet's center of figure must be obtained from an analysis of available immersion and emersion lightcurves. But because the separation of chords from various earth-based stations cannot exceed the earth's diameter, which is small compared with the giant planet's diameter, and because it is difficult to locate a standard point in the lightcurve (usually taken to be the half-flux point) with spatial precision much better than about $\sim 0.1 H$, where H is the refractivity scale height (about 60 km for Saturn), the location of the center of figure from groundbased occultation data can seldom be achieved with spatial precision better than ~ 10 km. The limits of precision in determining the center from fitting only to chords on a giant planet such as Saturn depend on the details of the distribution of the chords and on the availability of *a priori* information about the planet's atmo-

spheric shape. This situation is to be contrasted with that for an occultation of a spacecraft radio signal by a planetary atmosphere (e.g., Lindal *et al.* 1985), where the geometry is usually known to ~ 1 km from tracking of the Doppler residuals.

Groundbased observers were afforded a favorable geometry during the 28 Sgr occultation (Fig. 1); the star was unobstructed by Saturn's rings during all atmospheric immersion and emersion events save immersion from Chile, yet the near-central occultation of the star during an open ring presentation permitted measurement of some 18 sharp-edged circular ring features from multiple earth stations during both inbound and outbound passage. Solutions for the ring geometry by French *et al.* (1993) and Hubbard *et al.* (1993a) yielded a most important byproduct for the present analysis, namely a precise determination of the apparent path of 28 Sgr at each observatory with respect to the Saturn center of mass (presumed identical to the center of the figure).

In the present analysis, we make use of the same data sets used by Hubbard *et al.* (1993a), augmented by observations of immersion and/or emersion obtained at Lick Observatory, McDonald Observatory, the Infrared Telescope Facility (IRTF), Las Campanas Observatory (CLCO), and European Southern Observatory (ESO). Table I presents a summary of the 11 data sets contributing to this paper. Please see Nicholson *et al.* (1995), French *et al.* (1993), Hubbard *et al.* (1993a), and Harrington *et al.* (1993) for more details about individual observations.

Because of various problems encountered at some of the stations, the total number of immersion/emersion lightcurves available for analysis is 18 rather than 22, equally divided between immersion and emersion events.

We use two basic coordinate systems in this discussion, one aligned with the star-Saturn vector, and the other aligned with Saturn's symmetry axis. First we define a Cartesian coordinate system centered on Saturn for photons from 28 Sgr which are observed on the earth at time t : let the z -axis pass through 28 Sgr and the position of the center of Saturn at the time these photons were at Saturn, with z increasing in the direction of the star, and let the orthogonal x and y axes also pass through the center of Saturn, increasing to the celestial east and north respectively. In the same frame we place the observer, at $x = x'$, $y = y'$, and $z = -D'$ at time t , where D' is the distance from Saturn to the observer backdated for the light propagation time (Fig. 2). Even in the absence of appreciable atmospheric refraction the observer would measure the *apparent* projected star position at $x = x' + D'\epsilon_{G,x}$, $y = y' + D'\epsilon_{G,y}$ with respect to Saturn, where ϵ_G is the gravitational bending angle given by Eq. (10) of Hubbard *et al.* (1993). Saturn's gravitational focusing is substantial, deflecting the rays by ~ 30 km (about $1/2$ a Saturn atmospheric scale height) over the propagation distance D' to the shadow plane.

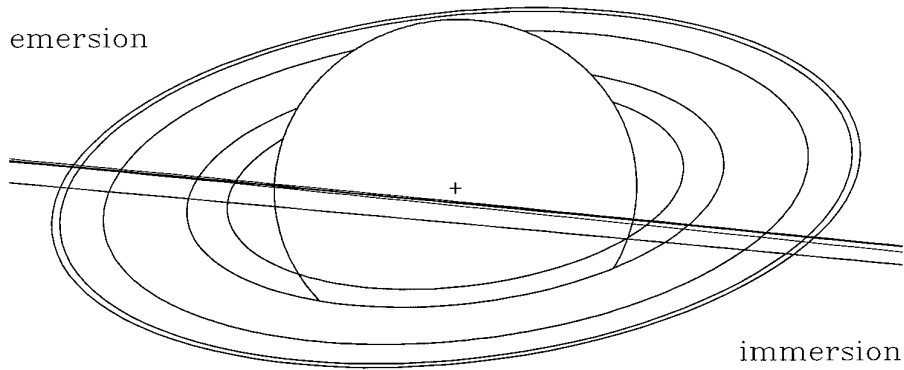


FIG. 1. Apparent tracks of 28 Sgr with respect to Saturn. The three Chilean stations correspond to the lowest chord plotted. The motion of the star was from right (west) to left (east).

The second basic coordinate frame is centered on Saturn and aligned with the symmetry axis. First, let \tilde{x} , \tilde{y} , \tilde{z} be a Cartesian frame with the \tilde{z} -axis aligned with Saturn's rotation axis and \tilde{x} , \tilde{y} lying in the equatorial plane with the \tilde{y} -axis toward the sub-earth meridian. The transformation from the x , y , z frame to the \tilde{x} , \tilde{y} , \tilde{z} frame is given by the angles P (position angle of Saturn's projected north pole) and B (latitude of the sub-earth point on Saturn); expressions for these angles are given by Hubbard *et al.* (1993a), and values for the geometrical parameters used in this paper are given in Table II.

We will also employ the spherical-polar coordinate system r , θ , φ , where r is the radius from the center of Saturn, θ is the angle from the rotation axis (colatitude), and φ is the longitude variable, which plays no role because of the assumption of axial symmetry. We also use a related cylindrical coordinate system, ℓ , \tilde{z} , φ , with $\ell = r \sin \theta$, the distance from the rotation axis.

In Fig. 12 of Hubbard *et al.* (1993a), the 80% confidence level ellipse for the position of Saturn's pole is shown; this ellipse maps into an ellipse in the x , y plane for the

uncertainty δx , δy of the projected position of the star with respect to the center of Saturn at any time t , for a given station (Fig. 3). That is, for a given pole right ascension and declination α_P , δ_P which lies on the 80% confidence level ellipse, there is a corresponding shift in the inferred position of the center of Saturn in the x , y plane; it is these shifts which are plotted in Fig. 3. As is evident, for this occultation, the geometry is known to approximately spacecraft-level accuracy. If we were to employ the pole determination of French *et al.* (1993) which uses both 28 Sgr and Voyager data, the error ellipse would be even smaller; in either case, uncertainty in the position of the center of Saturn can be considered negligible for the purposes of the present analysis.

We should note here that Baron *et al.* (1989) previously established the figure of Uranus from occultation chords that all used ring occultations to find the center of the planet, as we are doing here.

Our analysis is presented in this paper as follows. In Section 2 (following) we discuss procedures for representing the shape of Saturn's mesospheric layers. The shape

TABLE I
Station Parameters

Location	Code	Telescope	λ (μm)	Sampling rate (Hz)	Latitude	Longitude	Elevation (m)
Mt. Hamilton, CA	Lick	91 cm	0.85	1	37°20'18.0"	121°38'35.1" W	1235
Catalina Sta., AZ	Cat	1.54 m	3.40	10	32°25'0.7"	110°43'55.1" W	2510
San Pedro Mártir, BC	SPM	2.1 m	3.23	10	31°2'38.0"	115°27'47.0" W	2830
Kitt Peak, AZ	SOKP	2.3 m	2.33	2	31°57'47.0"	111°35'57.8" W	2076
Mt. Hopkins, AZ	MMT	MMT	3.17	10	31°41'19.6"	110°53'4.3" W	2608
Mt. Locke, TX	McD	2.7 m	2.1	5	30°40'17.7"	104°01'17.6" W	2075
Mauna Kea, HI	UKIRT	3.8 m	3.08	3	19°49'32"	155°28'23" W	4193
Mauna Kea, HI	IRTF	3.0 m	3.255	4	19°49'46"	155°28'29" W	4100
Las Campanas, Chile	CLCO	2.5 m	2.30	3	-29°0'11"	70°42'09" W	2280
La Silla, Chile	ESO	1 m	3.4	10	-29°15'23.99"	70°44'18.33" W	2321
Cerro Tololo, Chile	CTIO	4 m	3.40	50	-30°9'57.8"	70°48'53.6" W	2235

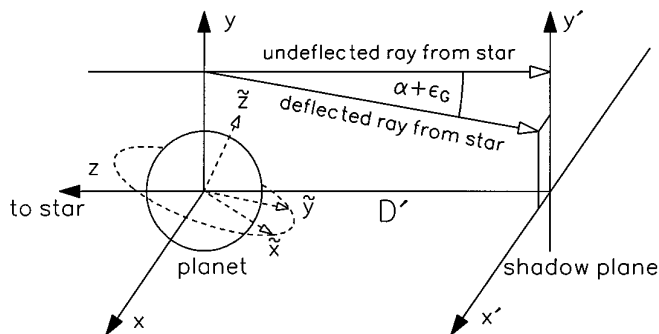


FIG. 2. Coordinate systems used in this analysis. In the case shown, the observer is located on the shadow plane at a finite y' and x' , observing a ray from the star passing through the x, y plane at $x = 0$ and $y > y'$, with closest-approach distance y to the planet. The ray is refracted through angle α and gravitationally deflected through a further angle ϵ_G . For nonspherical Saturn, the plane of deflection of such a ray would not contain the y and y' axes but would instead be defined by the x, y gradient of the integrated atmospheric phase shift (see Eq. (9)).

of these layers is primarily determined by mesospheric zonal winds, which can be determined only from the stellar occultation data and from extrapolations of cloud-motion data for Saturn's troposphere. In Section 3 we apply a simple two-parameter fitting procedure to each lightcurve to obtain the density scale height and values of x' , y' at a standard point in the lightcurve, in order to place constraints on Saturn's mesospheric shape in as model-independent a manner as possible. The results of this analysis strongly support the conclusion that tropospheric zonal winds continue into the mesosphere. Then, in Section 4, we use the derived mesospheric shape and various mesospheric structure models based upon average results from the analysis of Section 3 and upon Abelian inversions of the individual lightcurves to directly calculate synthetic immersion and emersion lightcurves for each station in our data set, and to compare the results of this global synthesis with the observed lightcurves. We present preferred mesospheric structure models in Section 4 at increasing levels of detail: (1) a mean-isothermal model based upon the analysis of Section 2; (2) a smooth polynomial-fit model based upon inversions; (3) an averaged inversion model. The latter two structure models are constrained by continuity with Voyager results for layers above and below the mesosphere.

TABLE II
Geometric Parameters

P (J2000.0 coordinates)	B	D'
6.2555°	25.4025°	1.3505×10^9 km

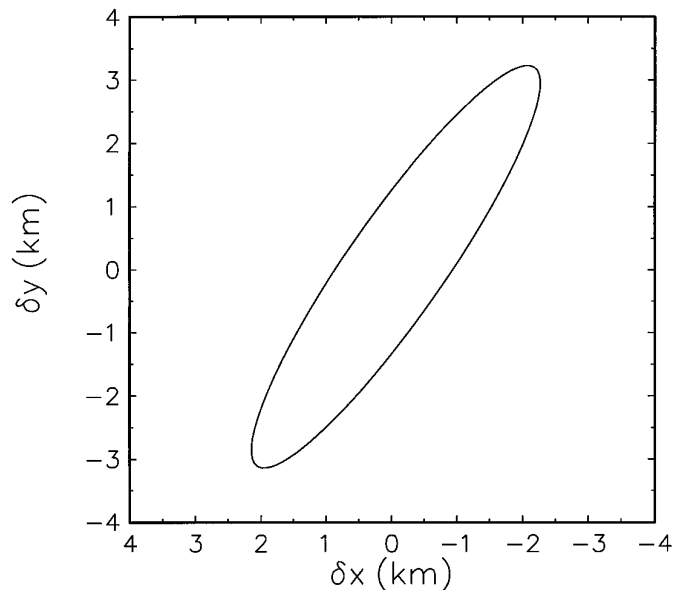


FIG. 3. The 80% confidence-level ellipse for the uncertainty in the position of Saturn's center, relative to the position of an earth station in the x, y, z frame at time t .

2. SHAPE OF SATURN'S ATMOSPHERE

Saturn's atmosphere is extremely nonspherical due to rapid rotation. The atmosphere also rotates with a variety of periods, which introduces substantial further deformation to the shape of level surfaces. In this paper, the assumed rotation periods are identical to those adopted by Nicholson *et al.* 1995; the data are from a personal communication from R. Beebe and N. Chanover. Measurements of the shape of Saturn's atmosphere at the 100-mbar pressure level from radio-occultation experiments of the Pioneer 11, Voyager 1, and Voyager 2 spacecraft showed clear evidence of the influence of zonal winds as well as the overall distortion of the planet due to its underlying solid-body rotation, presumed to correspond to the magnetic-field rotation period of 10.65667 h (Lindal *et al.* 1985). Our stellar-occultation data are able to provide information about Saturn's atmospheric shape at much higher altitudes, at pressures around a few microbars. An earlier analysis of central-flash data from 28 Sgr occultation observations (Nicholson *et al.* 1995) provided indications of some decay of zonal winds with height at the 2.5-mbar level, but at higher latitudes than those probed by the immersion and emersion events. In the present analysis, we find that the nonsphericity of Saturn's atmosphere due to zonal winds must also be taken into account at pressures of a few microbars, at latitudes close to the equator. Because the immersion/emersion levels are many scale heights above the levels near 1 bar where the wind speeds were actually measured, some approximation and extrapolation is re-

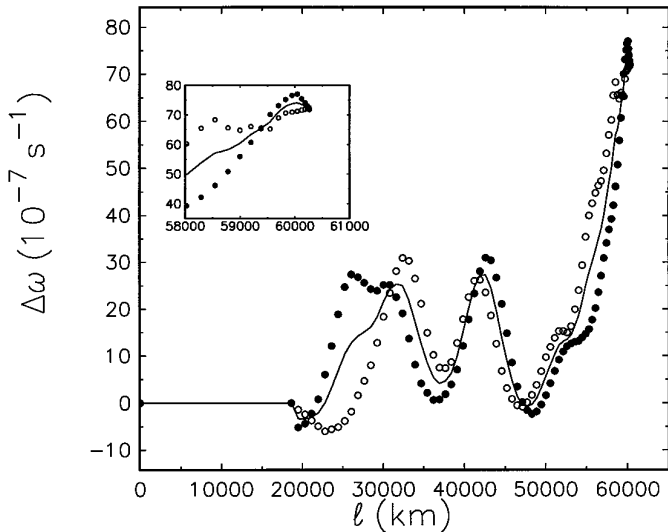


FIG. 4. Profile of differential rotation rates in Saturn's atmosphere measured from motions of clouds at pressures ~ 1 bar. Open circles are northern hemisphere rates; solid circles are southern hemisphere rates. The solid curve shows the mean of the two hemispheres for a given value of ℓ . Inset shows detail of behavior near the equator.

quired in order to construct a practical model for comparison with the data.

Let the magnetic-field rotation rate of Saturn be ω_0 . The zonal speed of a fluid element due solely to rotation at this rate is $v_0 = \ell\omega_0$, and amounts to about 10 km/s at Saturn's equator. At a given latitude, let the total zonal speed of a fluid element be $v_0 + \Delta v$, where $\Delta v = \ell\Delta\omega$ is the zonal wind speed with respect to the magnetic-field-stationary frame. Utilizing the Voyager-derived profile of Δv shown in Fig. 11 of Nicholson *et al.* (1995), we derive the profile for $\Delta\omega(\ell)$ shown in Fig. 4.

We have for the gravity vector \mathbf{g} observed by a fluid element in its comoving frame

$$g_\ell = \frac{\partial V}{\partial \ell} + \omega^2 \ell, \quad (1)$$

$$g_z = \frac{\partial V}{\partial z}, \quad (2)$$

$$g_\phi = 0, \quad (3)$$

where $\omega = \omega_0 + \Delta\omega$, V is the gravitational potential given by the solution to Poisson's equation $\nabla^2 V = -4\pi G\rho$, and G and ρ are the gravitational constant and mass density, respectively. We have assumed that only zonal flows exist and that they are time-independent, i.e., that Saturn's atmosphere is in a state of permanent differential rotation as defined by Tassoul (1978). In this case there exists a generalized equation of hydrostatic equilibrium $\nabla P = \rho\mathbf{g}$ relating the pressure P to the mass density ρ , and as is evident

from this equation, a surface of constant P is everywhere orthogonal to the local gravity \mathbf{g} . However, refractive occultation data are sensitive to the distribution of ρ rather than the distribution of P ; surfaces of constant ρ coincide with surfaces of constant P if and only if the atmosphere rotates on cylinders, i.e., ω is a function of ℓ only (Tassoul 1978).

As Fig. 4 makes clear, $\Delta\omega$ is not a function of ℓ only, and as a result the isobaric surfaces ($P = \text{const.}$) as given by solving the generalized equation of hydrostatic equilibrium cannot be north-south symmetric, nor can isopycnic surfaces ($\rho = \text{const.}$) coincide with isobaric surfaces. It is therefore necessary to introduce an *a priori* unknown temperature distribution to relate the isobaric surfaces to isopycnic surfaces.

We treat the problem of the unknown three-dimensional temperature distribution using two different approximations, with the expectation that the effect of the temperature distribution can be bounded by examining the differences between lightcurves computed using the two approximations.

Under the first approximation, surfaces of constant P , ρ , and temperature T coincide, and the calculation of the shape of these level surfaces can be obtained from potential theory: We symmetrize the distribution of $\Delta\omega(\ell)$ by performing a simple average of the north and south values for each value of ℓ , as shown by the solid line in Fig. 4. The resulting distribution is then assumed to be a function of ℓ only (the atmosphere rotates on cylinders). In this case, we may define for each location in the atmosphere a total effective potential $U = V + Q$, where V is the usual gravitational potential in free space (negligible ρ) given by

$$V = \frac{GM}{r} [1 - J_2(a_0/r)^2 P_2(\cos \theta) - J_4(a_0/r)^4 P_4(\cos \theta) - J_6(a_0/r)^6 P_6(\cos \theta)], \quad (4)$$

where M is the mass of Saturn, r is the radius from the center of mass, and J_n are the zonal gravity harmonics (Nicholson and Porco 1988, Campbell and Anderson 1989, Bosh 1994) normalized to a_0 , Saturn's equatorial radius at 1 bar (Lindal *et al.* 1985). In this paper we use the values of J_2 , J_4 , and J_6 obtained by Nicholson and Porco (1988), which for our purposes differ negligibly from the more recent determinations of these quantities (virtually all of the high-order shape variation at low latitudes is determined by zonal winds).

Our adopted parameters defining the gravitational figure of Saturn are given in Table III.

For rotation on cylinders, there exists a rotational potential

$$Q = \int_0^\ell \ell' d\ell' \omega^2(\ell'). \quad (5)$$

TABLE III
Gravitational Shape Parameters (Nicholson and Porco 1988)

a_0 (km)	J_2	J_4	J_6	ω_0 (s ⁻¹)	GM (cm ³ s ⁻²)
60268	16331×10^{-6}	-914×10^{-6}	108×10^{-6}	1.63778×10^{-4}	3.79406×10^{22}

The equation of hydrostatic equilibrium then reads $\nabla P = \rho \nabla U$; i.e., surfaces of constant U coincide with level surfaces.

We break Q into its uniform-rotation part, $Q_0 = \ell^2 \omega_0^2/2$, and a smaller part, ΔQ , which depends on the differential zonal rotation rates $\Delta\omega$. However, ΔQ is not known in all layers of Saturn's atmosphere which occulted 28 Sgr. These layers correspond to equatorial radii ~ 61000 km, i.e. several hundred km above the 1-bar level. Since the emersion occultations occurred very close to the equator, an extrapolation of ΔQ is required.

The extrapolation is based on the value of $d \Delta Q/d\ell$ at the largest value of ℓ for which it can be determined. We have $d \Delta Q/d\ell = [2v_0 \Delta v + (\Delta v)^2]/\ell \approx 2v_0 \Delta v/\ell$ since v_0 is much greater than Δv at Saturn's equator. We first take Δv to be constant with height at Saturn's equator, which implies an essentially constant value of $d \Delta Q/d\ell$ in the outer few percent of Saturn's equatorial radius. This linear extrapolation of ΔQ with ℓ for $\ell > 60,268$ km corresponds to our baseline model for the zonal winds in Saturn's equatorial mesosphere.

A second model, which we will denote “ ΔQ^- ” in the following, represents an extreme model where $d \Delta Q/d\ell$ vanishes in equatorial layers above the 1-bar level. This means that Δv vanishes in these layers. A third model, denoted as “ ΔQ^+ ,” assumes that $d \Delta Q/d\ell$ jumps by a factor 1.8 for ℓ above the 1-bar level. In this model, the equatorial

zonal wind is larger than the Voyager-measured values by this same factor of 1.8 for all values of ℓ above the 1-bar level, which would give equatorial zonal wind speeds on the order of 0.7 km/s in Saturn's equatorial mesosphere. The factor of 1.8 is chosen so as to *increase* the wind-induced height variation of level surfaces near the equator by roughly the same amount (~ 10 km) as it is *decreased* in the ΔQ^- model. As we discuss in the following, the baseline model is compatible with the 28 Sgr data and the ΔQ^+ model is marginally compatible, but the ΔQ^- model is not.

Under an alternative approximation, we do not symmetrize the distribution of $\Delta\omega(\ell)$ and do not assume the applicability of potential theory. Instead, we take the same approach as Nicholson *et al.* (1995): We utilize Eqs. (1)–(3) to compute the gravity \mathbf{g} at each point in the atmosphere, extrapolating the nonsymmetrized $\Delta\omega(\ell)$ to values of $\ell > 60,268$ km as needed. The shape of isobaric surfaces is then rigorously given by the solution to $\nabla P = \rho \mathbf{g}$ (as is also true in the case of symmetrized $\Delta\omega$). The approximation enters when one replaces isobaric surfaces with isopycnic surfaces for the purpose of modeling the lightcurves. This introduces an asymmetry between the north and south isopycnic surfaces which is not present in the symmetrized version, as well as introducing an inconsistency in any inferred temperature distribution defined only on isobaric surfaces. However, as we discuss below, the differences between

TABLE IV
Baum–Code Fits to Atmosphere Occultation Data (values of T computed with $\mu = 2.135$)

Event	$t_{1/2}$ (UT s)	H/v_\perp (s)	v_\perp (km/s)	H (km)	$\delta\phi_{\text{rms}}$	$a'_{1/2}$ (km)	$a_{1/2}$ (km)	g (cm/s ²)	Latitude (°)	T (K)	Δa (km)
IRTF immersion	24,898.5 \pm 0.47	2.66 \pm 0.19	20.96	55.8	0.078	60,876	60,971	901	-15.20	129	12
McD immersion	24,655.6 \pm 0.43	2.81 \pm 0.17	21.04	59.2	0.082	60,865	60,964	897	-14.19	136	4
SPM immersion	24,708.1 \pm 0.34	2.94 \pm 0.14	21.03	61.9	0.065	60,855	60,956	898	-14.13	143	-4
SOKP immersion	24,688.7 \pm 0.49	2.70 \pm 0.23	21.03	56.8	0.062	60,869	60,965	897	-14.09	131	6
Lick immersion	24,725.4 \pm 0.57	2.58 \pm 0.26	20.99	54.3	0.079	60,857	60,950	896	-13.82	125	-9
CTIO emersion	30,396.7 \pm 0.56	-3.07 \pm 0.20	-20.02	61.4	0.067	60,869	60,968	870	0.41	137	8
CLCO emersion	30,393.7 \pm 0.88	-2.95 \pm 0.27	-20.03	59.2	0.111	60,855	60,952	870	0.50	132	-8
UKIRT emersion	30,772.2 \pm 0.54	-3.17 \pm 0.21	-20.61	65.3	0.067	60,853	60,957	874	5.71	146	-3
McD emersion	30,527.5 \pm 0.63	-3.17 \pm 0.24	-20.61	65.4	0.078	60,848	60,951	874	6.04	147	-9
MMT emersion	30,558.5 \pm 0.52	-3.06 \pm 0.24	-20.63	63.1	0.085	60,875	60,977	875	6.21	142	17
SOKP emersion	30,560.5 \pm 0.37	-3.24 \pm 0.14	-20.64	66.9	0.066	60,848	60,953	875	6.24	150	-7
SPM emersion	30,577.1 \pm 0.60	-3.40 \pm 0.22	-20.65	70.2	0.074	60,844	60,953	875	6.24	158	-7
Cat emersion	30,557.7 \pm 0.54	-3.39 \pm 0.21	-20.63	70.0	0.085	60,862	60,970	875	6.25	157	10
Lick emersion	30,606.6 \pm 0.50	-3.07 \pm 0.20	-20.65	63.3	0.071	60,848	60,949	875	6.63	142	-11
average				62.3			60,960			141	0
std. dev.				4.8			9			10	5
prob. error				± 1			± 2			± 3	

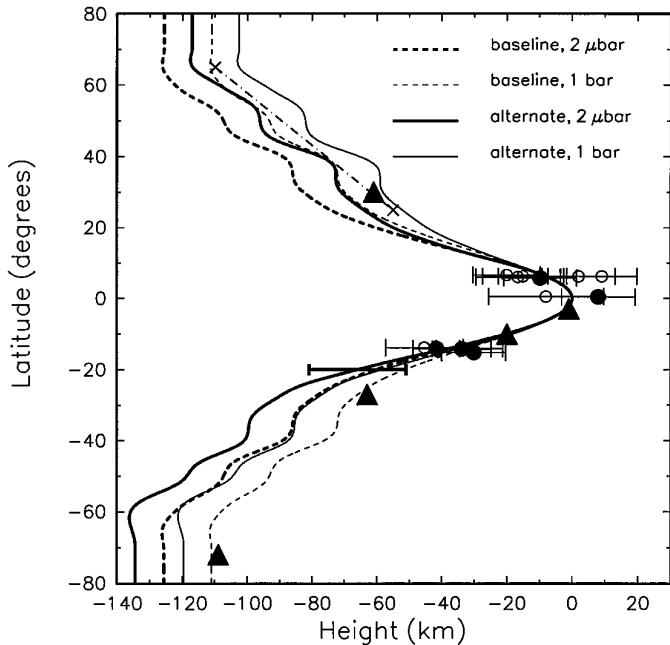


FIG. 5. Shape of Saturn's atmosphere at 1 bar (light curves) and extrapolated to $2 \mu\text{bar}$ (heavy curves) using the baseline model (dashed), and the alternate model with north-south differences (solid). The abscissa is the height of a given pressure level using a given differential rotation model above the radius of that same pressure level computed using the uniform rotation rate ω_0 . Triangles are determinations at 100 mbar from Pioneer 11 and Voyager 1 and 2 radio-occultations. The dot-dashed line segment ending in crosses shows the best-fit model of Nicholson *et al.* (1995) from 28 Sgr central flash data. Solid dots correspond to our highest-quality lightcurves, SPM, McD, and IRTF immersion, and CTIO and UKIRT emersion; open circles are data from lightcurves of lower quality. The error bar without a dot at -20° latitude represents limits placed on the shape from modeling the ring-obscured immersion at the three Chile stations (which was calculated from a full three-dimensional simulation without using Baum-Code theory).

lightcurves synthesized with the first approximation and those synthesized with this alternative approximation are barely perceptible, and do not affect our final conclusions in any way.

3. BAUM-CODE FITS

In this section we present a simple model-fitting approach to the occultation data set. Our objective here is to constrain the shape of Saturn's limb and determine whether the data set can be characterized by a single consistent temperature, based upon a model with a minimum number of parameters. We fit each lightcurve with a Baum-Code lightcurve $\phi(t)$ which depends on the two parameters $t_{1/2}$ and H/v_\perp (Baum and Code 1953). Here ϕ is the instantaneous stellar flux normalized to its unocculted value, $t_{1/2}$ is the time at which $\phi = 1/2$, H is the atmosphere's refractivity scale height (assumed constant), and v_\perp is the

component of the star's velocity perpendicular to the atmosphere's level surfaces projected onto the sky (x, y) plane. Baum-Code theory assumes that the atmosphere is spherical with radius $a_{\text{eff}} \gg H$. The normalized Baum-Code flux is $\phi = 1/(1 + D'\alpha/H)$, where α is the total angle of refraction of the ray from the star to observer. If r is the incident ray's distance from the z -axis in the x, y plane of Fig. 2 (closest-approach distance to the planet) and r' is the refracted ray's distance from the z -axis in the x', y' (shadow) plane, then $r' = r - D'(\alpha + \varepsilon_G)$ (the small-angle approximation is excellent since neither α nor ε_G exceeds $\sim 10^{-7}$). At $\phi = 1/2$, clearly $D'\alpha = H$, so we calculate the corresponding value of r using $r = r' + H + D'\varepsilon_G$. Baum-Code theory also gives, for the refractivity $\nu_{1/2}$ at the point of deepest penetration into the atmosphere, $D'\nu_{1/2}/H = \sqrt{H/2\pi a_{\text{eff}}}$. Our problem is to find a method by which to apply these relations, valid for a spherically symmetric atmosphere, to Saturn's nonspherical atmosphere.

In the general case, for a ray passing through Saturn's nonspherical atmosphere with closest-approach coordinates x, y and refracted through angle α with components α_x, α_y before reaching an observer at coordinates $x', y', z = D'$, we have (including gravitational bending)

$$x' = x - D'\alpha_x - D'\varepsilon_{G,x} \quad (6)$$

and

$$y' = y - D'\alpha_y - D'\varepsilon_{G,y}. \quad (7)$$

The plane of refraction does not in general include the z -axis.

Baum-Code theory is applied to the nonspherical saturnian atmosphere as follows. For a given station, the apparent path of the star with respect to the center of Saturn is given by $x'(t), y'(t)$, and is known from the astrometric solution. These numbers do not include gravitational deflection or refraction of the rays by Saturn. Using the potential-theory approach (north-south-averaged symmetry), we construct a table of level surfaces for Saturn's atmosphere for a given model of Q by solving the implicit equation $U(r, \theta) = U(a, \pi/2)$ to obtain the function $r = r(\theta)$ at fixed a , for a grid of values of the equatorial radius a ranging from 60,200 to 61,500 km. The table is then transformed into the x, y, z frame. For a given vacuum stellar position x', y' , a search is then made along z to find a_{min} , the minimum value of a for the level surfaces traversed by the undeflected ray. Let this value be a' , which will play the role of r' in the spherically-symmetric Baum-Code problem. That is, if the ray were undeflected, it would probe to the deepest level surface labeled by the parameter a' . But because of refraction and gravitational deflection, the deepest level actually probed by the ray must be calculated from x, y given by Eqs. (6) and (7). An

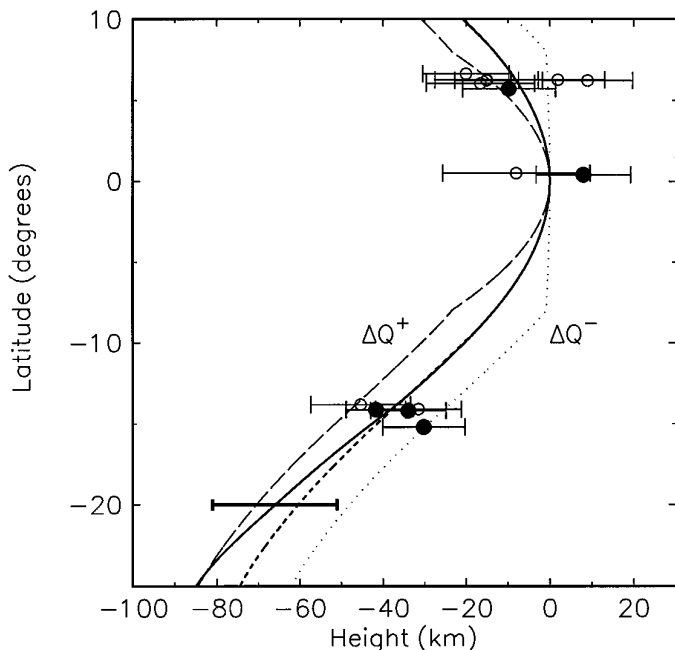


FIG. 6. Magnified view of the equatorial region of Fig. 5, together with shape profiles for models ΔQ^- and ΔQ^+ . Only the shape at the 2 μ bar pressure level is shown. The ΔQ^- model does not fit the data shown in this figure (we calculated χ^2 for each of the four models shown here and obtained $P(\chi^2|15) = 0.8, 0.8, 0.2,$ and 0.07 for the baseline, alternate, ΔQ^+ , and ΔQ^- models respectively, where P is the probability that random variations would give a larger value of χ^2).

accurate calculation of this level requires allowance for the components $\alpha_x, \alpha_y, \varepsilon_{G,x}, \varepsilon_{G,y}$, via Eqs. (6) and (7), as well as the finite value of B , which moves the point of deepest penetration out of the x, y plane. We provide an exact treatment of these issues in Section 4. For the purpose of the present discussion, we reduce the nonspherical Saturn atmosphere to a spherical approximation by assuming that at the point where $\phi = 1/2$, we have

$$D'\alpha = H, \quad (8)$$

where $\alpha = \sqrt{\alpha_x^2 + \alpha_y^2}$. Under this approximation, the deepest level surface probed by the ray is then labeled by a , where $a = a' + D'\alpha + D'\varepsilon_G$, and $\varepsilon_G = \sqrt{\varepsilon_{G,x}^2 + \varepsilon_{G,y}^2}$.

In summary, the nonspherical atmosphere is represented in the Baum–Code problem by the following substitutions: $r' \rightarrow a', r \rightarrow a$, and evidently, $v_\perp \rightarrow da'/dt$, where v_\perp is the rate at which the level surfaces are being traversed by the star (in the absence of refraction). Note that because we label the level surfaces with their equatorial radius a' or a , extrapolation of the atmospheric wind speeds to values of ℓ greater than 60,268 km is an essential element in this procedure, since all of the 28 Sgr events traverse level surfaces which lie in this range.

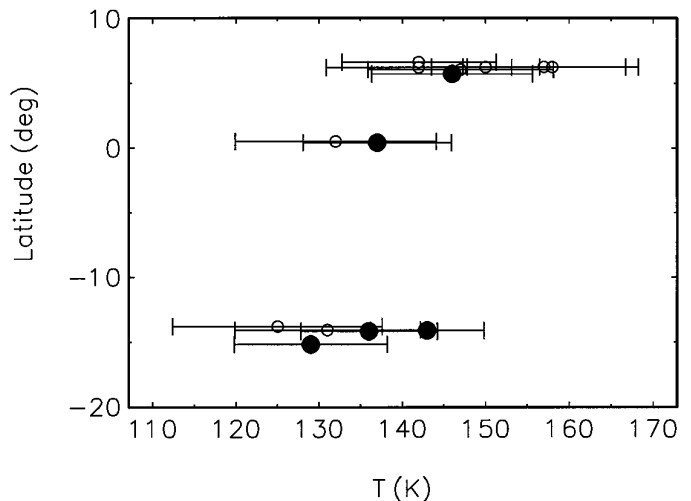


FIG. 7. Temperature vs. latitude at the half-flux level, as derived from Baum–Code fits.

We must consider the validity of the approximation given in Eq. (8), since the plane defined by the net bending components $(\alpha_x + \varepsilon_{G,x}), (\alpha_y + \varepsilon_{G,y})$ does not in general contain the projected radius vector from the center of Saturn defined by the components x, y . However, the difference is slight for all the events considered here, which occurred at latitudes no greater than 20° from the equator. In this latitude range, the angle between the normal to Saturn’s limb (which contains the bending plane to high precision) and the radius vector from the center of Saturn, projected in the sky plane, is no more than about 2° . The cosine of this angle differs negligibly from unity.

Two further approximations must be considered. First, v_\perp is not rigorously constant during the occultation, but varies in a complex manner which depends on the latitude of the stellar image in Saturn’s atmosphere and on the extrapolation of the shape of level surfaces into the stratosphere. However, we find that the variation is smaller than 10 m/s over the interval of ϕ considered here, and thus v_\perp can be adequately represented by a constant mean value over that interval. Second, the Baum–Code problem assumes that the value of r is identical to the radius of curvature of the atmosphere in the refraction plane, but because of Saturn’s oblateness, the effective radius of curvature in the refraction plane a_{eff} will in general differ from a except

TABLE V
Derived Parameters at Half-Flux Level

$\nu_{1/2}$	$n_{1/2} \text{ (cm}^{-3}\text{)}$	$P_{1/2} \text{ (}\mu\text{bar)}$
$(6.07 \pm 0.14) \times 10^{-10}$	$(1.25 \pm 0.03) \times 10^{14}$	2.43 ± 0.08

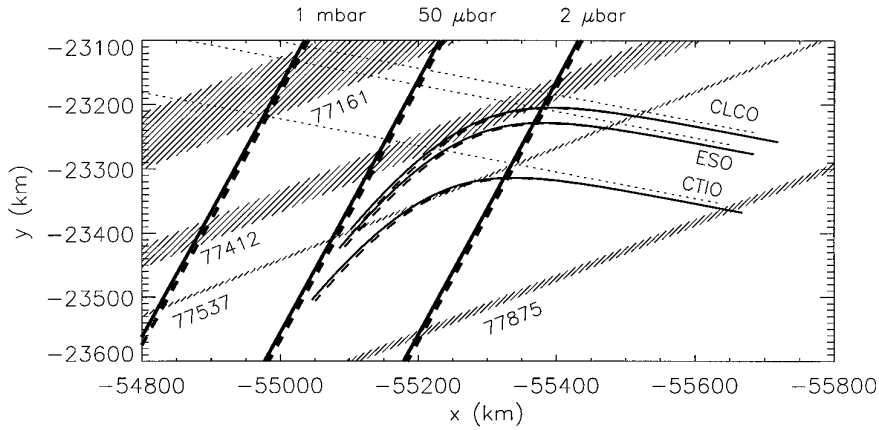


FIG. 8. Immersion geometry for Chile stations (cf. Fig. 1). The difference between the vacuum star positions (dotted lines) and the refracted stellar image positions (curved lines) at the start of the interval, prior to any atmospheric refraction (right side), is caused by gravitational deflection of the rays. As is evident in this figure, the difference in positions of atmospheric pressure levels and image positions for the baseline wind model (*dashed*) and the alternate wind model (*solid*), is very slight, amounting to only a few km.

in the case of an equatorial occultation with $B = 0$. Thus Baum–Code theory will give a value for the gas density along the refraction path which is too small by a factor $\sqrt{a_{\text{eff}}/a}$.

Table IV summarizes results of Baum–Code fits to lightcurves, using the baseline model for Q in Saturn’s high atmosphere. As we discuss below, differences in radial scale introduced when we use the alternative model with north–south wind differences, amount to at most a few km and are therefore negligible for our purposes. Table IV does not include immersion at the three Chile stations, where the star was obstructed by C-ring features, nor does it include a partial Catalina observation of emersion. The IRTF and UKIRT at Hawaii respectively observed immer-

sion and emersion only. The MMT failed to obtain data at immersion, and the ESO emersion experiment was foiled by poor guiding due to differential refraction in the earth’s atmosphere. In Table IV, the two parameters of the Baum–Code fit are given along with probable errors for each. These parameters were determined for each lightcurve by fitting to 75 s of data beginning a few seconds before immersion or terminating a few seconds after emersion. Times given in Table IV are seconds after 00h UTC on 3 July 1989.

Since fitting a Baum–Code model to the data is a nonlinear regression problem, our determination of the probable errors requires some discussion. First, we determined $\delta\phi_{\text{rms}}$, the r.m.s. scatter of the data with respect to the

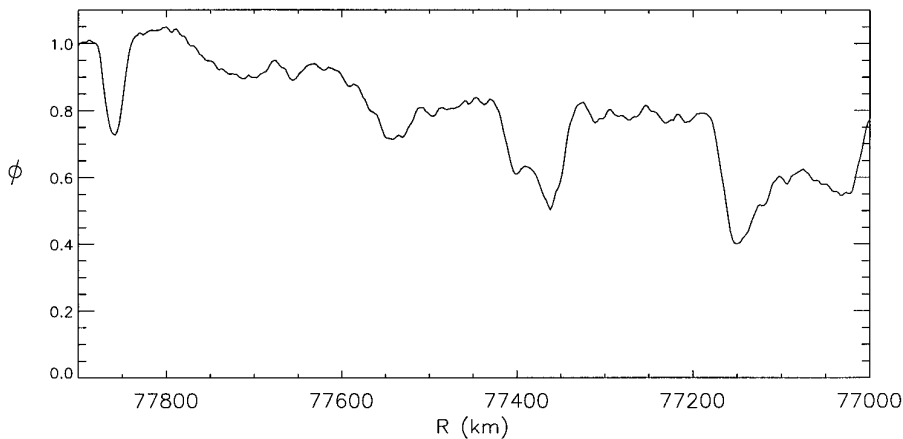


FIG. 9. Normalized stellar flux ϕ plotted versus projected ring-plane radius R , for SPM inbound (time runs from left to right). The slight elevation of ϕ above unity just inside the eccentric ring feature at $R = 77,875$ km is caused by Fraunhofer diffraction of starlight from small ring particles scattering extra starlight into the beam. Interestingly, when we compare our best-fit models of immersion at the Chile stations with the data, we find that the Fraunhofer diffraction is absent, as if the atmosphere has quenched it.

best-fit Baum–Code lightcurve (its value is given in Table IV for each station). Then, a series of artificial lightcurves was produced by superimposing on the best-fit Baum–Code lightcurve a random noise component with a Gaussian distribution and an r.m.s. scatter equal to the observed value. The correlation time for the random noise was set equal to 1 s, the approximate time to traverse the projected stellar diameter of 18 km (Hubbard *et al.* 1993a). The scatter in the derived Baum–Code parameters from fitting to each of these artificial lightcurves was then used to estimate the probable errors. While the dominant source of noise in the lightcurves is scintillations in Saturn's atmosphere, which are neither Gaussian-distributed nor constant along the lightcurve, we believe that this procedure provides a consistent and valid determination of the uncertainty in the inferred parameters. Note, however, that stations whose chords are within a few hundred km of each other in the x' , y' plane have correlated fluctuations in ϕ during either immersion or emersion, and thus their measured scale heights may show less dispersion than the estimated uncertainty in a given measurement.

We then determined v_{\perp} and $a'_{1/2}$, the value of a_{\min} at $t_{1/2}$, using the procedures given above; the corresponding $a_{1/2}$ is given by $a_{1/2} = a'_{1/2} + H + D'\varepsilon_G$ in accordance with Eq. (8). At the coordinates \tilde{x} , \tilde{y} , \tilde{z} corresponding to $a_{1/2}$, i.e., at the intersection of the ray at $\phi = 1/2$ with the deepest level surface, we compute the total local gravity g , the latitude $90^\circ - \theta$, and then the local temperature using $T = \mu g H / R$, where $\mu = 2.135$ is the mean molecular weight (Lindal *et al.* 1985) and R is the gas constant. The final column in Table IV gives Δa , which for each station is the difference of $a_{1/2}$ from the mean value of 60,960 km. The equatorial height of the half-flux level ($a_{1/2}$) above the 1-bar level (a_0) is determined to be 692 km with an uncertainty of a few km.

Both the baseline model and the alternate model for the shape of Saturn's atmosphere at $a = 60,960$ km fit the data very well. The situation is summarized in Fig. 5, which shows the calculated shape of Saturn's atmosphere as a function of latitude for two pressure levels, compared with data. In this plot, the abscissa is the height of the differentially rotating model above the radius of a uniformly rotating model with the same equatorial radius a and at the same pressure level. The uniformly rotating model rotates at the magnetic field rotation rate.

Figure 6 shows an expanded view of the central portion of Fig. 5, with our 28 Sgr data only. As is evident, our data

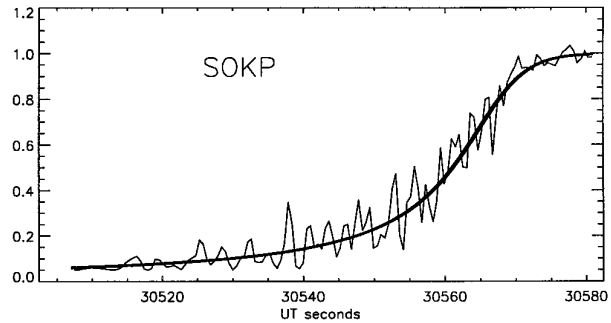
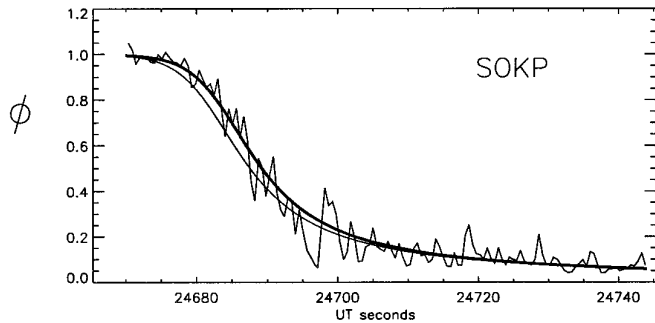
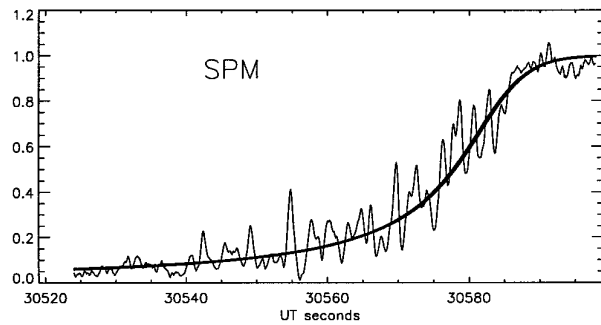
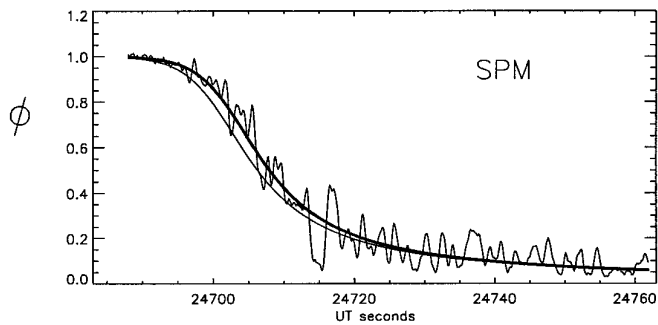
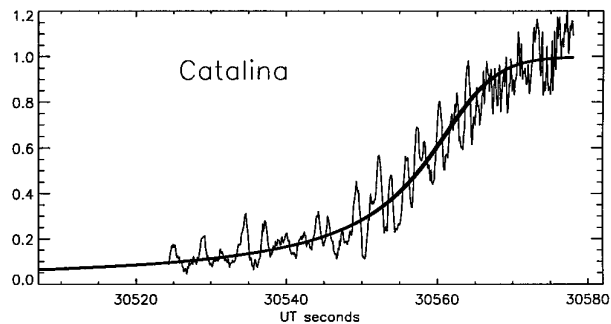
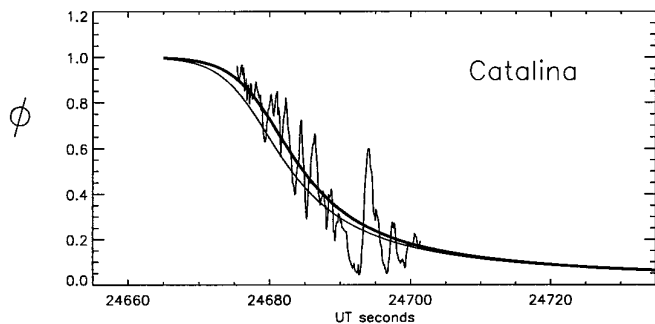
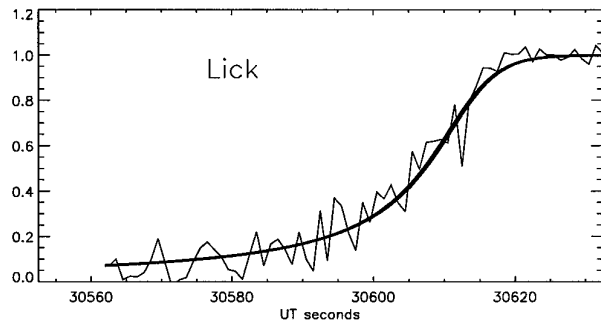
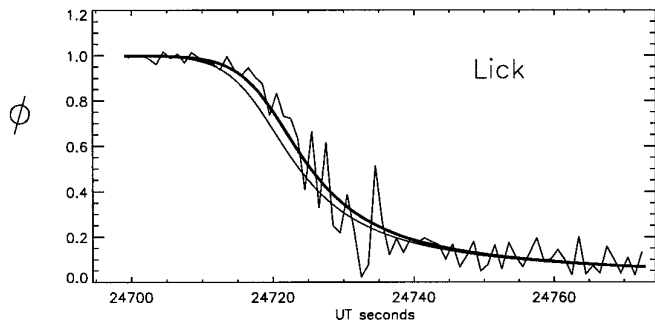
set span a radial range in the wind-induced equatorial bulge equal to a full scale height, and thus strongly confirm its presence in Saturn's high atmosphere. We do not have data at latitudes beyond $\pm 20^\circ$, where the bulge should continue to drop by another scale height. However, our consistency with the radio-occultation height scale for Saturn's atmosphere, discussed below, supports the absolute as well as the relative radial position of the stellar-occultation points. Both Fig. 5 and Fig. 6 show the calculated radius differences obtained both by using potential theory and by solving the equation of hydrostatic equilibrium for the isobaric surfaces and assuming that they correspond to isopycnic surfaces, using the full nonsymmetrized $\Delta\omega(\ell)$.

Figure 7 shows temperature as a function of latitude inferred from the fits listed in Table IV, with error bars propagated from the error bars in H/v_{\perp} . This figure shows no evidence for any latitude dependence of T at the 2.4- μ bar level. The slightly higher temperatures for the points clustered near $+6^\circ$ latitude should not be considered significantly different from those measured at other latitudes because these points are affected by correlated density fluctuations in Saturn's atmosphere and thus have correlated scintillations, the main source of noise in the inferred temperature.

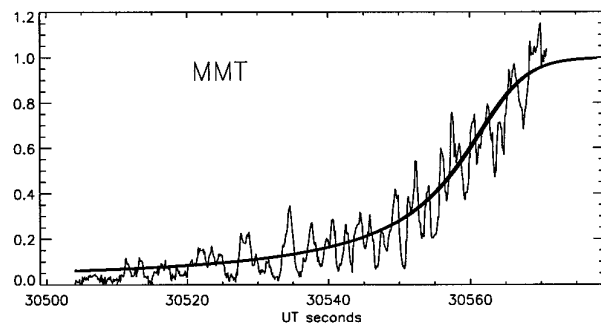
For the wavelengths used in these observations, we have adopted a refractivity at standard temperature and pressure ν_{STP} , for a mixture of hydrogen and helium with $\mu = 2.135$, of $\nu_{\text{STP}} = 1.30 \times 10^{-4}$ (Elliot *et al.* 1974). Table V gives further results derived from Baum–Code fits shown in Table IV, values at the half-flux level for the refractivity $\nu_{1/2}$, number density $n_{1/2}$, and pressure $P_{1/2}$. These numbers include a correction factor of $\sqrt{a/a_{\text{eff}}}$ which we calculated as follows: We numerically determined the phase of the ray (see Eq. (9) immediately below) at the half-flux point and used Baum–Code theory to calculate the value of a_{eff} which would give that phase. For the immersion and emersion points of the 28 Sgr events, and taking into account the value of B , a representative value is $a_{\text{eff}} = 57,230$ km, which results in values for $\nu_{1/2}$, $n_{1/2}$, and $P_{1/2}$ which are about 3% larger than the values which would be inferred by setting $a_{\text{eff}} = a_{1/2}$.

Not all of the Baum–Code approximations could be expected to be valid over an unrestricted range of latitudes for a highly oblate planet such as Saturn. However, for the near-equatorial latitudes probed by the 28 Sgr events, the theory works well. We checked the validity of this assertion by synthesizing light curves for an atmosphere

FIG. 10. Immersion and emersion data (irregular curves) compared with the $T = 141$ K isothermal model (smooth heavy curve), starting with the northernmost station (Lick) and continuing south. The heavy curve is computed using the baseline model for ΔQ (the alternate rotation model gives virtually the same lightcurves). The lighter smooth curve shows an isothermal model with $\Delta Q = 0$ everywhere, i.e., for a model of Saturn's upper atmosphere with no differential rotation.



MMT immersion
not observed



isothermal at $T = 141$ K and with the other best-fit parameters given in Tables IV and V, using the exact theory given in Section 4. We then compared these lightcurves with Baum–Code lightcurves for the same parameters. The agreement was excellent.

4. MODELING OF LIGHTCURVES

4.1. Direct Problem

We employ a numerical algorithm for computing a theoretical model of $\phi(t)$ for an arbitrary 3-dimensional distribution of refractivity $\nu(\tilde{x}, \tilde{y}, \tilde{z})$. The disadvantage of this approach is that it is inherently more demanding of numerical precision than are approaches which approximate the planetary atmosphere with an effectively spherically symmetric distribution of ν , but the advantage is that complicated transformations from curvilinear coordinate systems are not required.

We begin with the values x', y' for the ray's endpoint. Making a guess for the corresponding x, y using Eqs. (6) and (7), we numerically evaluate the ray's phase,

$$\Phi = k \int_{-\infty}^{\infty} dz \nu(x, y, z) \quad (9)$$

(k is the photon wavenumber). Setting up a grid of points in the vicinity of x, y , we numerically evaluate the bending angle components:

$$\alpha_x = -\frac{1}{k} \frac{\partial \Phi}{\partial x}; \quad (10)$$

$$\alpha_y = -\frac{1}{k} \frac{\partial \Phi}{\partial y}. \quad (11)$$

Given x', y' , the coordinates x, y are recomputed from Eqs. (6) and (7). This cycle is continued until converged. Note that in general there will be more than one point x, y which satisfies Eqs. (6) and (7) for a given x', y' . For example, in a spherically-symmetric planet, one solution has x, y close to x', y' compared with a_0 , and the other solution has x, y at the opposite limb, about $2a_0$ away. Because we deal only with the first 75 s of occultation, we are solely concerned with the near-limb raypath in this paper, and so no attempt is made to locate more than the one (near-limb) raypath for a given value of x', y' . Strictly speaking, if the bending angle α changes sufficiently rapidly with depth in the atmosphere, raypaths may cross and more than one near-limb image can appear. But in the

direct calculations carried out in this analysis, we use distributions of ν which are sufficiently smooth for this not to occur.

Once the raypath has been determined, the flux is then calculated using

$$\begin{aligned} \phi &= \frac{\partial(x, y)}{\partial(x', y')} \\ &= \left[1 - D' \left(\frac{\partial \alpha_x}{\partial x} \right)_y - D' \left(\frac{\partial \alpha_y}{\partial y} \right)_x \right. \\ &\quad \left. + D'^2 \left(\frac{\partial \alpha_y}{\partial y} \right) \left(\frac{\partial \alpha_x}{\partial x} \right) - D'^2 \left(\frac{\partial \alpha_x}{\partial x} \right) \left(\frac{\partial \alpha_y}{\partial y} \right) \right]^{-1}. \end{aligned} \quad (12)$$

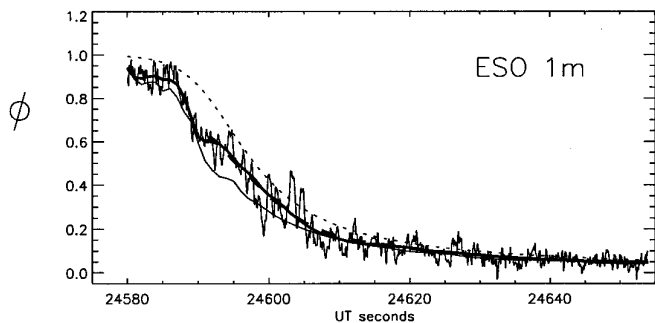
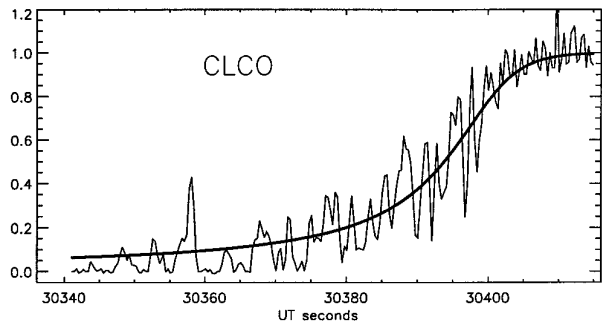
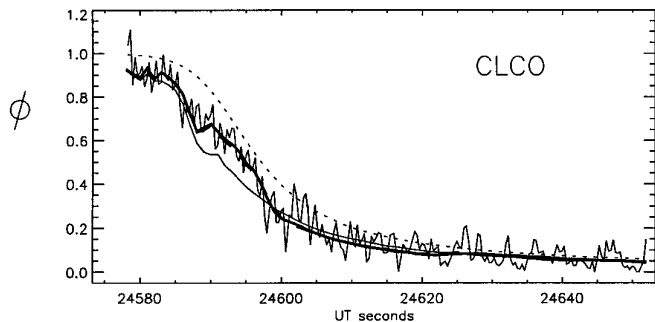
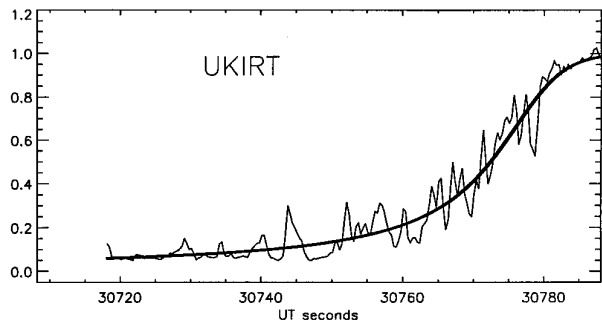
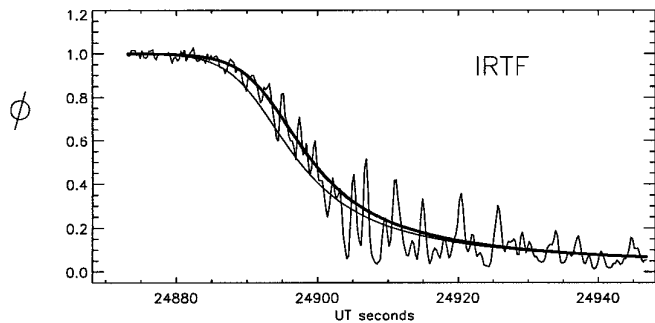
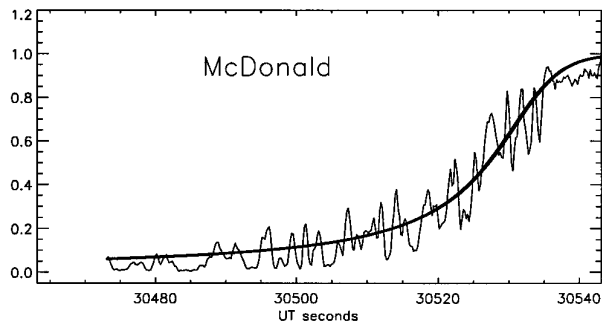
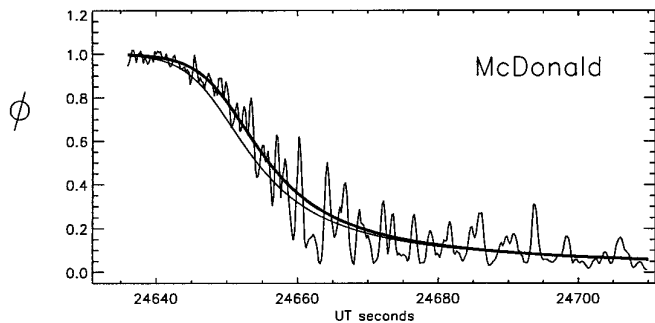
The “gravitational-lensing” components of ϕ due to the terms in ε_G are so small for this geometry that they can be safely neglected.

On the boundary between regions where the number of raypaths increases or decreases (caustic), Eq. (12) diverges. Such a boundary would include the Saturn central flash region investigated by Nicholson *et al.* (1995). But since we limit our modeling to layers where x', y' is close to the projected limb, no such divergences are encountered.

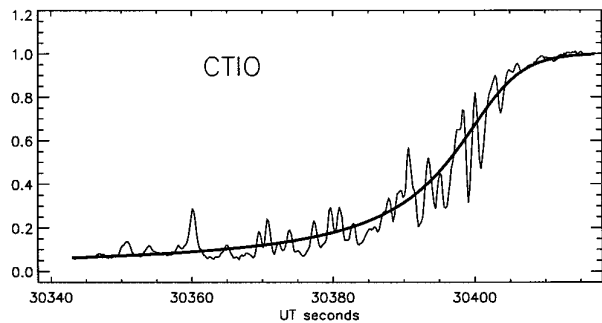
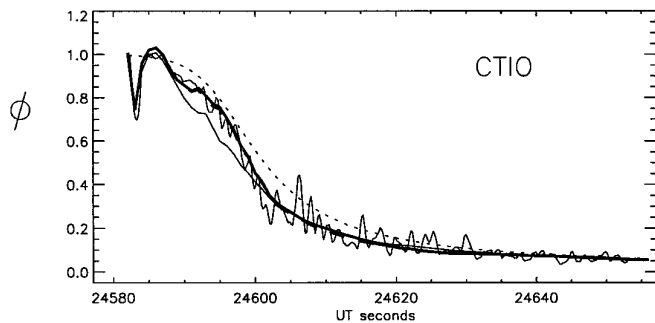
The accurate evaluation of the second derivatives of Φ encountered in Eq. (12) presents some challenges. We performed this task by setting up an appropriate grid in x, y . In practice, an interval between mesh points equal to about 15 km, or $H/4$, proved to give adequate precision for reasonably smooth distributions of ν .

Calculation of a complete set of lightcurves for all stations, for a given atmospheric model, took about five hours on a Sun Sparc 20 workstation, with the precise time required depending on the complexity of the atmospheric model and the resulting requirements on the mesh size. We first solved the direct problem of calculation of a strictly isothermal model at $T = 141$ K, with $n = n_{1/2}$ at $a = a_{1/2}$ (values from Table IV). For each station, the value of x', y' was then supplied to the above algorithm at 75 values of t separated by 1 s (one correlation time), distributed with respect to the immersion or emersion time as previously described. We used the baseline model for Q in the occultation layers. We integrated the equation of hydrostatic equilibrium to obtain $\nu(\ell, \tilde{z}) = \nu(a)$ for $T = 141$ K. Note that we included allowance for variation of H with ℓ and \tilde{z} due to variable gravity, as well as precise treatment of the nonspherical geometry, so this model made none of the approximations of the Baum–Code treatment. In particu-

FIG. 11. Same as Fig. 10, continuing south. The three Chile immersions have been modeled with C-ring material. Dotted curves for Chile immersion show isothermal lightcurves (baseline model for ΔQ) without C-ring material.



ESO 1m emersion
not observed



lar, the only free parameters of the calculation were T and n at $a = 60,960$ km; the time of atmospheric immersion or emersion at each station was completely fixed by the model.

In the direct problem we also synthesized lightcurves for the three Chile immersion stations. This calculation required the use of a model for the opacity of the intervening C-ring features. Figure 8 shows the relevant geometry for this part of Saturn's limb. The dotted curves show x' , $y'(t)$ for standard 75-s intervals at each station. The solid curves show, for the $T = 141$ K isothermal model and for the alternate wind model, the corresponding trajectories of x , $y(t)$ as the stellar image moves from west (right) to east (left), contacts the atmosphere, and begins to move along the limb toward the south. The shaded bands are loci of C-ring features projected on the x , y -plane; each feature is labeled with its outer radius in km in the equatorial plane. A final set of loci (labeled with pressures) show projected contours of constant a_{\min} . For the baseline model (north-south symmetry with rotation on cylinders), the stellar image trajectories and projected pressure levels move to the loci shown as dashed lines. The convention for distinguishing between baseline model and alternate model for Saturn's isopycnic surfaces is the same as that used in Figs. 5 and 6.

Although Fig. 8 gives the impression that the star passed through some clear regions in the C-ring during immersion, in fact there was material present during virtually of the immersion interval. To model this complicated distribution of opacity, we used our best record of C-ring features, the lightcurve obtained at SPM (Fig. 9).

Synthesis of a lightcurve at one of the Chile immersion stations involved the following additional steps beyond the ones outlined above. First, at a given $x(t)$, $y(t)$, the projected radial position of the stellar image in the equatorial plane R was computed. Then, at that value of R , the stellar flux ϕ for SPM inbound was evaluated and set equal to the projected transmission of the C-ring material at this point. Finally, the total value of ϕ for a given Chile station was obtained by multiplying the value of ϕ for purely refractive defocusing by this transmission factor.

Note that atmospheric refraction caused the 77,537-km feature to be crossed twice during immersion at CLCO and ESO, and to be grazed at CTIO. Note also that because the relevant C-ring features are not azimuthally symmetric or time-independent, we could not use emersion profiles or spacecraft profiles to model them. But by using a trace from SPM which cuts across the features at a point which is separated in azimuthal distance along the rings from the Chile crossings by a distance small compared with the distance over which significant radial variation of C-ring features would occur, we believe that we have a valid determination of the relevant ring transmission factors for Chile immersion.

With the rings corrected for in the three Chile immersion lightcurves, we then used both the baseline model (rotation on cylinders) and the alternate model (north-south asymmetric) to compute an ensemble of immersion and emersion lightcurves for all data sets, for an isothermal atmosphere with only two parameters: $T = 141$ K and total number density $n = 1.253 \times 10^{14}$ cm $^{-3}$ on the level surface with equatorial radius $a = a_{1/2} = 60,960$ km (from Tables IV and V). Lightcurves for both models are plotted in Figs. 10 and 11, using the same convention as in Fig. 8—dashed curve for the baseline model, solid curve for the alternate model. But the dashed lightcurves cannot be seen in Figs. 10 and 11 because they lie almost exactly on top of the solid lightcurves; that is, the difference in the two models is insignificant for the purpose of modeling the lightcurves.

The isothermal model provides a good fit to all the data. This is to be expected, since the Baum-Code results shown in Table IV are tightly clustered around a mean temperature of 141 K. The close agreement of the data and the synthesized lightcurves shown in Figs. 10 and 11 confirm the validity of the geometrical approximations in Section 3 which were used to apply spherically symmetric Baum-Code theory to Saturn's nonspherical atmosphere.

Figures 10 and 11 also show theoretical lightcurves (lighter solid curves) for the identical isothermal model atmosphere (same number density at equatorial radius $a = 60,960$ km), but with no zonal winds included, that is, with $\Delta Q = 0$. This would be a rigorous solution to the hydrostatic equilibrium equation using Eqs. (1)–(3) with $\omega = \omega_0$ in Eq. (1), i.e., with $v = 0$ in the mesosphere. Our data are incompatible with such a constant-temperature, windfree solution.

It should be noted that the CLCO lightcurves are affected by a nonlinearity in the detection device which cannot be completely calibrated. Thus some vertical mismatch between theory and data for CLCO is expected, although the times of occurrence of sudden changes in signal level should be valid. Also note that because only a partial lightcurve was observed during Catalina immersion, the vertical scale is less certain.

Immersion lightcurves are particularly sensitive to the equatorial "topography" induced by differential zonal flows (Figs. 5 and 6). The strong mismatch which occurs when these flows are neglected leaves no doubt that this topography is present at stellar occultation levels in the vicinity of $a = 60,960$ km.

4.2. Inverse Problem

We now turn to the problem of determining what additional atmospheric structure, beyond the mean temperature at the half-flux level, can be determined from the 28 Sgr data. For this purpose, we use an iterative procedure to determine the distributions $\nu(a)$ and $T(a)$ which are

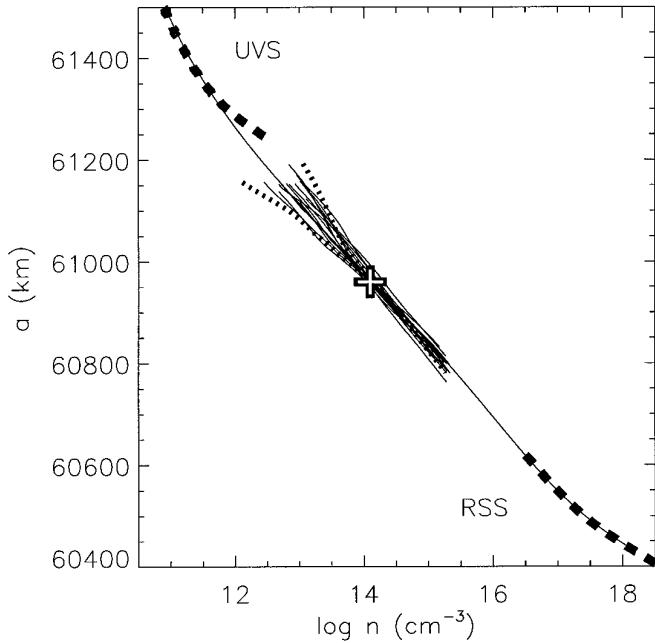


FIG. 12. UVS and RSS data (*heavy dashed curves*) for $n(a)$, together with 28 Sgr inversions. The two *dotted* inversions are obtained using extreme starting conditions, for SOKP emersion (upper) and CTIO emersion (lower). *Cross* is plotted at the half-flux level, using the mean values from Baum–Code fits (Tables IV and V). *Solid curve* passing through all data is model L, obtained from a least-squares fit.

compatible with the stellar occultation data, available spacecraft data, and the constraint of hydrostatic equilibrium. Spacecraft data for Saturn’s atmosphere include the UVS experiment employing ultraviolet occultation measurements in the high atmosphere (above $a = 61,200$ km; Smith *et al.* 1983) and RSS (radio-occultation) measurements below $a = 60,600$ km (Lindal *et al.* 1985). In the case of the RSS experiment, the altitude scale was computed with a zonal wind model essentially equivalent to the one used here, and all results were given as a function of a , the corresponding equatorial radius of the level surface, as is done here.

The UVS altitude scale was obtained in a way that differed somewhat from the technique used here, leading to moderate systematic differences. The δ Sco stellar occultation occurred at 3.9° N latitude and the solar occultation at 29.5° N latitude. The Voyager UVS investigators related the altitude scales for these two observations by computing equipotential surfaces for an equilibrium figure using the gravitational field and *uniform* rotation with the magnetic-field rotation period. They adopted $a_0 = 60,263$ km, close to the value used here. The corresponding 1-bar levels for the δ Sco and solar occultations were then found to be at $r = 60,239$ and $58,598$ km, respectively. The effect of the zonal winds included in the present calculation would be to increase the difference between these two radii by about

TABLE VI
Coefficients for
Eq. (15)

i	A_i
0	14.1374215
1	-5.88446712
2	-0.434277268
3	3.53694268
4	2.06467931
5	-5.10523485
6	2.11465365
7	-0.141397900

70 km. The Voyager UVS investigators then related the observed lightcurves to computed altitudes above the respective 1 bar levels by obtaining the geometrical impact parameter for the line of sight as a function of Spacecraft Event Time from the spacecraft trajectory and the known positions of the star and sun; this gave a one-to-one relationship between the occultation lightcurves and the altitude. The procedure was essentially identical to that used for the δ Sco ring occultations except that the impact parameter in the latter case was computed for the ring plane.

UVS temperature and number density profiles are shown graphically as a function of equatorial radius; we digitized these for our purposes using automatic curve-following software.

We first computed a set of profiles of $\nu(a)$ and then $n(a)$ for the occultation lightcurves using standard inversion procedures (e.g., Wasserman and Veverka 1973; French *et al.* 1978). As is well known, such profiles are obtained by starting with the outermost point of the lightcurve where ϕ first starts to drop below unity and working to deeper levels. The $n(a)$ profiles are sensitive to the assumed initial density as well as to the influence of atmospheric layers above the starting point. This problem could be mitigated by making use of a reliable $n(a)$ profile from the UVS data. However, as we discuss below, the UVS profile in layers just above the stellar-occultation layers is not easily reconciled with our data and a reasonable model atmosphere.

We obtained inversion profiles by using techniques appropriate for radially symmetric atmospheres, making the approximation $v_\perp = da'/dt$ evaluated at $\phi = 1/2$. The total refractive angle α in the spherical approximation was computed using the radially symmetric version of Eq. (12), neglecting the term in ε_G :

$$D' d\alpha = (\phi^{-1} - 1) dr', \quad (13)$$

and after integrating, we solved for r using

$$r = r' + D'\alpha, \quad (14)$$

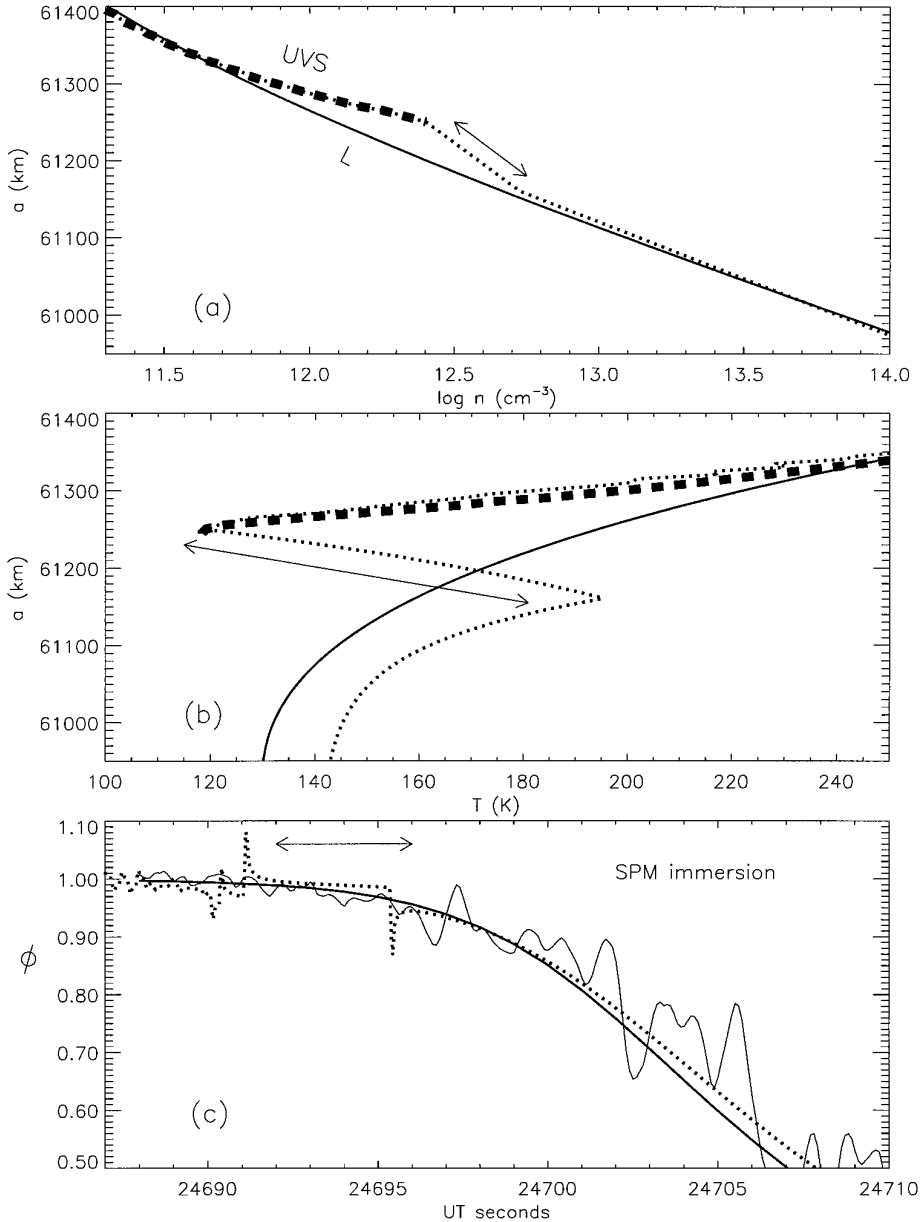


FIG. 13. Properties of a model compatible with an isothermal structure for $a < 61,160$ km and the entire UVS profile (*dotted curve*), compared with model L. (a) The interpolation in $n(a)$, with the interpolation indicated by arrows. (b) The resulting temperature profile (*solid curve* is model L). (c) Comparison of synthetic lightcurves for the interpolation model (*dotted curve*) and a full three-dimensional calculation for model L (*solid curve*), compared with SPM immersion data. The half-flux time $t_{1/2}$ can vary by up to ~ 1 s (about 20 km in a), depending on the details of the atmospheric model above the half-flux radius at $a = 60,960$ km.

making the spherical approximation $r' \rightarrow a'$, $r \rightarrow a$. The refractivity distribution was then obtained by applying an Abel inversion to the radially symmetric version of Eqs. (9)–(11). As discussed in Section 3, the resulting refractivities were then multiplied by a factor $\sqrt{a/a_{\text{eff}}}$, with $a_{\text{eff}} = 57,230$ km, to allow for an atmospheric radius of curvature equal to a_{eff} in the refraction plane.

As is well known, the integration of Eq. (13) must start

at some finite radius, and the refractivity at that point in the atmosphere is finite but unknown from the occultation data. Our initial inversion solutions were computed using the following procedure (cf. French *et al.* 1978): We started the inversion in each lightcurve at a point where $1 - \phi$ was significantly larger than the noise in the data. Typically, this was at about $\phi = 0.95$. Call this point ϕ_S . We assumed that ϕ_S was given by a Baum–Code solution at this point

TABLE VII
Model L + inv; Best Fit to Atmosphere Occultation Data

a (km)	$\log n$ (cm ⁻³)	g (cm s ⁻²)	T (K)	P (μ bar)
61,500	10.9102	848.9	357.5	0.004012
61,490	10.9446	849.3	351.2	0.004267
61,480	10.9799	849.7	344.6	0.004543
61,470	11.0163	850.0	337.9	0.004843
61,460	11.0536	850.4	331.0	0.005169
61,450	11.0919	850.8	323.9	0.005525
61,440	11.1312	851.2	316.8	0.005915
61,430	11.1716	851.5	309.5	0.006343
61,420	11.2130	851.9	302.2	0.006813
61,410	11.2556	852.3	294.8	0.007331
61,400	11.2991	852.6	287.5	0.007903
61,390	11.3438	853.0	280.2	0.008537
61,380	11.3897	853.4	272.9	0.009241
61,370	11.4366	853.8	265.7	0.01002
61,360	11.4846	854.1	258.7	0.01090
61,350	11.5338	854.5	251.7	0.01188
61,340	11.5840	854.9	244.9	0.01297
61,330	11.6354	855.3	238.3	0.01421
61,320	11.6880	855.6	231.8	0.01560
61,310	11.7416	856.0	225.6	0.01717
61,300	11.7963	856.4	219.5	0.01896
61,290	11.8521	856.7	213.7	0.02099
61,280	11.9090	857.1	208.1	0.02329
61,270	11.9670	857.5	202.7	0.02593
61,260	12.0260	857.9	197.5	0.02895
61,250	12.0860	858.2	192.6	0.03241
61,240	12.1470	858.6	187.9	0.03639
61,230	12.2091	859.0	183.4	0.04099
61,220	12.2721	859.4	179.2	0.04629
61,210	12.3360	859.7	175.2	0.05243
61,200	12.4009	860.1	171.4	0.05956
61,190	12.4666	860.5	167.9	0.06785
61,180	12.5331	860.9	164.5	0.07749
61,170	12.6005	861.2	161.3	0.08877
61,160	12.6686	861.6	158.4	0.1019
61,150	12.7375	862.0	155.6	0.1174
61,140	12.8071	862.4	153.0	0.1355
61,130	12.8773	862.8	150.6	0.1568
61,120	12.9481	863.1	148.4	0.1818
61,110	13.0196	863.5	146.2	0.2112
61,100	13.0929	863.9	143.6	0.2455
61,090	13.1719	864.3	140.4	0.2879
61,080	13.2509	864.6	137.4	0.3379
61,070	13.3298	865.0	134.8	0.3978
61,060	13.4088	865.4	132.8	0.4697
61,050	13.4877	865.8	132.0	0.5600

TABLE VII—Continued

a (km)	$\log n$ (cm ⁻³)	g (cm s ⁻²)	T (K)	P (μ bar)
Layers Constrained by Sgr Occultation				
61,040	13.5540	866.2	132.9	0.6571
61,030	13.6225	866.5	133.9	0.7753
61,020	13.6946	866.9	134.1	0.9167
61,010	13.7674	867.3	134.0	1.083
61,000	13.8395	867.7	134.1	1.279
60,990	13.9102	868.0	134.6	1.510
60,980	13.9793	868.4	135.4	1.782
60,970	14.0464	868.8	136.6	2.098
60,960	14.1133	869.2	137.7	2.468
60,950	14.1801	869.6	138.8	2.900
60,940	14.2469	869.9	139.6	3.404
60,930	14.3141	870.3	140.2	3.988
60,920	14.3836	870.7	140.2	4.681
60,910	14.4539	871.1	139.6	5.481
60,900	14.5279	871.5	138.7	6.456
60,890	14.6004	871.8	137.9	7.583
60,880	14.6731	872.2	137.1	8.918
60,870	14.7473	872.6	136.4	10.52
60,860	14.8197	873.0	136.0	12.40
60,850	14.8914	873.4	136.0	14.63
60,840	14.9621	873.8	136.3	17.25
60,830	15.0315	874.1	136.9	20.31
Interpolation to RSS Data				
60,820	15.1009	874.5	137.4	23.92
60,810	15.1704	874.9	137.8	28.16
60,800	15.2399	875.3	138.2	33.14
60,790	15.3093	875.7	138.5	38.99
60,780	15.3788	876.1	138.8	45.85
60,770	15.4482	876.4	139.1	53.90
60,760	15.5177	876.8	139.3	63.36
60,750	15.5872	877.2	139.5	74.46
60,740	15.6566	877.6	139.7	87.49
60,730	15.7261	878.0	139.9	102.8
60,720	15.7956	878.4	140.1	120.7
60,710	15.8650	878.7	140.2	141.8
60,700	15.9345	879.1	140.3	166.6
60,690	16.0040	879.5	140.4	195.6
60,680	16.0734	879.9	140.6	229.8
60,670	16.1429	880.3	140.7	269.8
60,660	16.2124	880.7	140.8	316.8
60,650	16.2818	881.0	140.8	372.0
60,640	16.3513	881.4	140.9	436.8
60,630	16.4207	881.8	141.0	512.8
60,620	16.4905	882.2	140.8	601.2
60,610	16.5632	882.6	140.3	708.6
60,600	16.6334	883.0	140.3	832.4
60,590	16.7022	883.4	140.7	978.2
60,580	16.7697	883.8	141.1	1146
60,570	16.8401	884.1	140.8	1344
60,560	16.9150	884.5	139.5	1583
60,550	16.9914	884.9	138.0	1868
60,540	17.0665	885.3	137.0	2203
60,530	17.1410	885.7	135.7	2591
60,520	17.2223	886.1	133.4	3071
60,510	17.3080	886.5	130.1	3650
60,500	17.3977	886.9	126.3	4356
60,490	17.4925	887.2	122.0	5232

with a scale height equal to the mean scale height given in Table IV. Then the initial bending angle $\alpha_s = H(\phi_s^{-1} - 1)/D'$, and the initial refractivity was computed from the Baum–Code value corresponding to α_s . This procedure of course introduced considerable noise in the initial inversion, but when averaged over our multiple lightcurves, the noise was suppressed. Likewise, any uncertainty in the starting values for ν_s was suppressed at deeper layers in the inversion.

Figure 12 shows UVS and RSS profiles for $n(a)$, along with individual profiles for each of the 14 lightcurves which we could reduce using the above procedure. To illustrate the effect of the unknown starting density and temperature on the inversions of 28 Sgr data, we show with dotted lines two extreme $n(a)$ profiles, computed using starting temperatures 40% higher than 140 K and 40% lower, which yield lightcurves to match data at two of our stations. The solid curve which passes through the UVS, 28 Sgr, and RSS data was obtained by performing a least-squares fit (in $\log n$) of a polynomial with the form

$$\log n = \sum_{i=0}^7 A_i [(a - a_{1/2})/a_{1/2}]^i, \quad (15)$$

with data points weighted to force a fit to the UVS and RSS data at a chosen level of precision and for chosen intervals. Note that the large decrease in scale height for the UVS data for $a < 61,300$ km is anomalous, and would require substantial curvature in the $n(a)$ relation in this region. We therefore provisionally assumed that the UVS $n(a)$ relation was valid for $a > 61,400$ km, but not at lower altitudes. The solid curve which was obtained by this latter fitting procedure, and which is shown in Fig. 12, is denoted model L (for least-squares), and provides as good a fit to the 28 Sgr data as the isothermal model. The coefficients for model L, to be used in expression (15), are given in Table VI. The polynomial fit is valid in the interval $60,428 < a < 61,995$ km.

4.3. Comparison with UVS Data

Next, we carried out an investigation to determine whether the implied “kink” in the $n(a)$ profile, should the UVS profile be valid for $a < 61,300$ km, is compatible with the 28 Sgr data. Figure 13a shows a model in which $\log n$ vs a is linearly interpolated from the last UVS data point to our best-fit isothermal ($T = 141$ K) atmosphere at $a = 61,160$ km, where the first effects of atmospheric refraction appear in the lightcurves. Such an interpolation has a drastic effect on the temperature profile, as shown in Fig. 13b. This effect is demanded by the equation of hydrostatic equilibrium and the specified height difference and density change. However, the resulting lightcurve shown in Fig. 13c is not greatly distorted because the interpolation is in a region where the gas density is so low that there is as yet little refraction. Thus, based on comparison with our occultation data alone, there is no reason to reject the UVS profile of $n(a)$ in the interval $61,225 < a < 61,350$ km. However, our accurate absolute altitude scale below

the interpolation region requires a fairly abrupt change of slope for $\log n$ vs a in the interpolation region and a corresponding violent temperature oscillation there. Since there is no physical reason to expect, on a planetary scale, such a temperature oscillation in this altitude range, a reasonable alternative is to use a smooth interpolation such as the L model.

4.4. An Average Model Based on Inversions

The L model fits the 28 Sgr data as well as the isothermal model, but is more physically reasonable because it takes into account the Voyager UVS and RSS data. However, the L model by its nature filters out any atmospheric structures on vertical scales smaller than ~ 300 km. Since the 28 Sgr data set has an unusually large number of individual occultation lightcurves, it is possible to exploit this large number to investigate whether any finer-scale structures survive a process of suitably averaging over the individual occultation profiles.

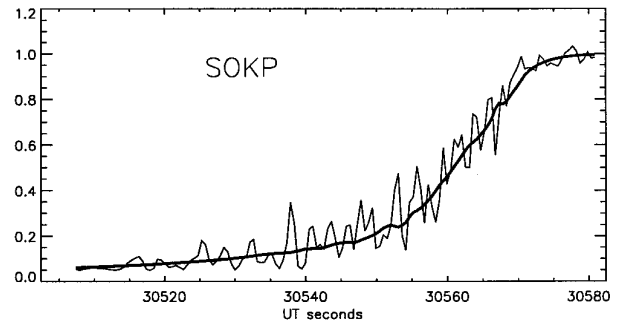
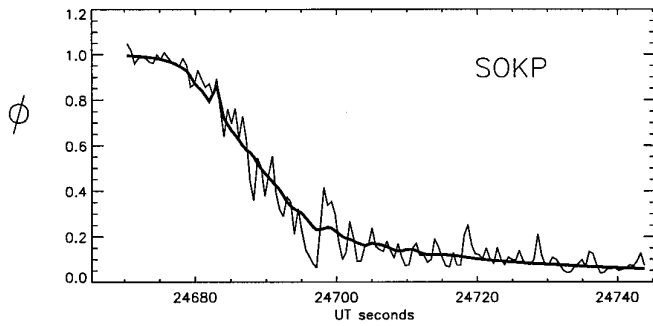
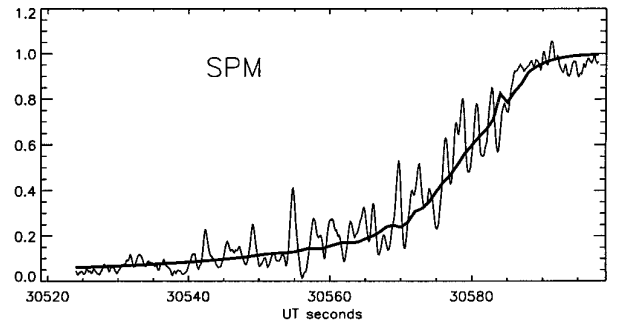
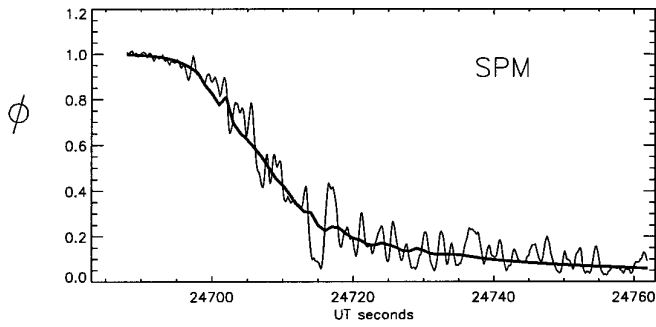
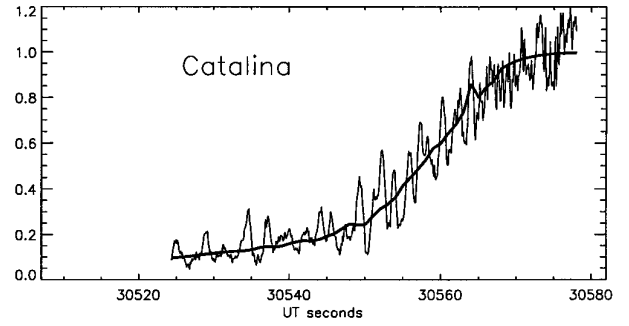
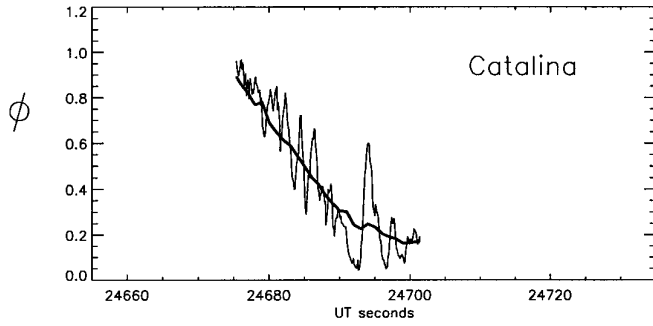
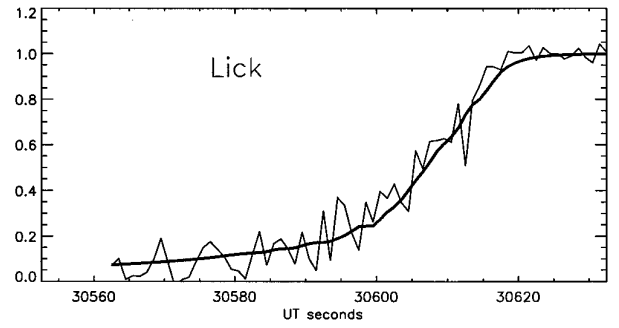
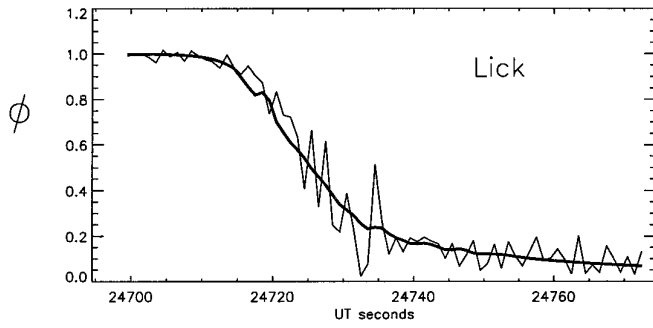
The averaging process is as follows. Starting with the inversions described above, we take the individual $n(a)$ profiles at each value of a , and perform a simple average of the $\log n$ values. This averaging is more meaningful than an average over n because the inversions give values of n at a given altitude which vary by substantial factors (see Fig. 12), and a process of averaging over n would unphysically bias the result to the larger values of n . This averaging process gives an $n(a)$ profile which is compatible with the L model at the upper end, and which can simply be continued as the L model at higher altitudes. The extension to lower altitudes is performed by linearly interpolating in $\log n$ vs a between the highest RSS point and the lowest averaged inversion point. The resulting model, which we denote as L + inv, is presented in tabular form in Table VII. Note that the middle range of Table VII, for $60,830 \leq a \leq 61,040$ km, is obtained by the process of averaging inversions of 28 Sgr lightcurves; the remainder of Table VII represents interpolations to UVS and RSS data.

Model L + inv retains some small-scale density fluctuations which survive the averaging process, but these may not be significant, although they do produce some small-scale features which show up in many of the lightcurves. Figures 14 and 15 show a comparison of model L + inv with the data.

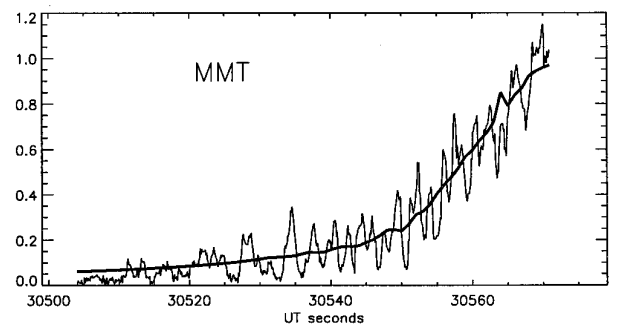
4.5. Summary of Models

Figure 16 shows, on the T vs a plane, three models which fit the 28 Sgr data. The two models discussed above, L and L + inv, are tied to the Voyager profiles at higher and

FIG. 14. Similar to Fig. 10; data are compared with the L + inv model (smooth heavy curve), using the baseline rotation model.



MMT immersion
not observed



lower altitudes. However, we have also examined a third model of the type proposed by Yelle *et al.* (1996) for Jupiter, in which an isothermal mesosphere lies below a zone with a steep outward temperature increase. Yelle *et al.* parametrize the temperature distribution in the form

$$T(a) = T_0 + \frac{T_\infty - T_0}{1 + e^{-\alpha(a-a_m)}}, \quad (16)$$

where T_0 (= 141 K in the present case) is the mesosphere temperature, T_∞ (= 420 K if we adopt the UVS topside temperature) is the asymptotic temperature at high altitude, and α is related to the maximum temperature gradient, which occurs at a_m . For Jupiter, Yelle *et al.* find that a_m corresponds to pressures of 0.3 to 0.5 μ bar. These same pressures occur in Saturn at $a \approx 61,080$ km. Accordingly, we adopted two ‘‘Jupiter-like’’ models with $a_m = 61,080$ km and a maximum temperature gradient of 1 K/km (model Y1) and 5 K/km (model Y5). The large temperature gradient in Y5 produces a large oscillation in the lightcurves for $\phi \approx 0.8$ which is not seen in our data. However, model Y1 (shown in Fig. 16) yields lightcurves that fit our data very well.

5. CONCLUSIONS

We have derived an optimized Saturn mesospheric model based upon UVS, RSS, and 28 Sgr occultation data. Although these data sets are not overlapping, the gaps are so small that the atmospheric structure is closely constrained. An important element in deriving the model is establishment of an absolute height scale for level surfaces in Saturn’s nonspherical atmosphere, since a height interval between two level surfaces at specified densities provides a constraint on the mean temperature in that interval, by the equation of hydrostatic equilibrium. Note also that the mean mesospheric temperature which we infer from occultation data is directly proportional to the assumed mean molecular weight. Gautier and Owen (1989) report a helium/hydrogen number ratio in Saturn’s atmosphere of (0.2 ± 0.1) times the solar value; with allowance for a small amount of methane, this leads to the value of $\mu = 2.135$ adopted here. If Saturn’s helium abundance were much closer to the solar value, our inferred mean mesospheric temperature would rise from 141 K to about 153 K.

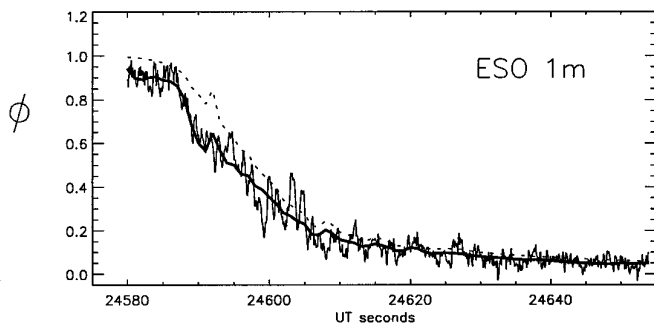
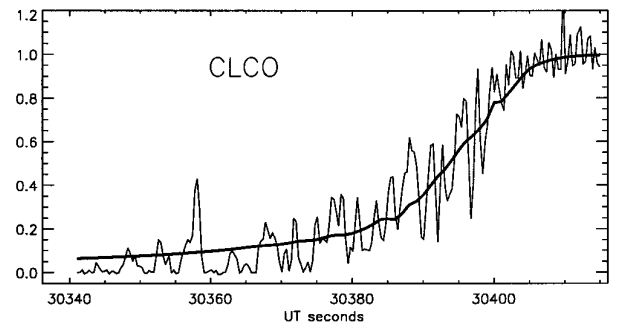
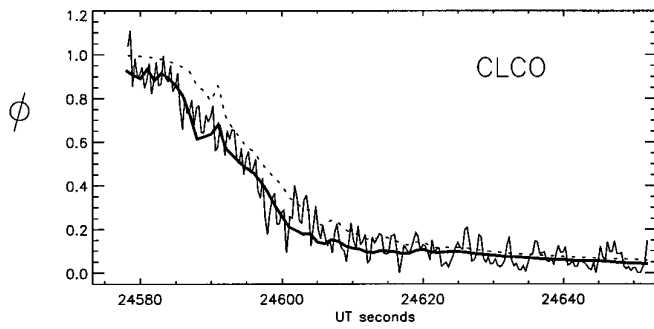
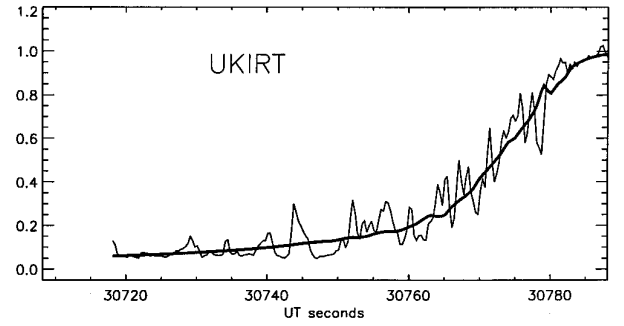
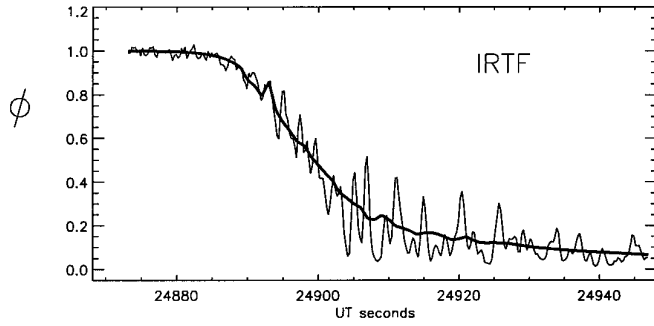
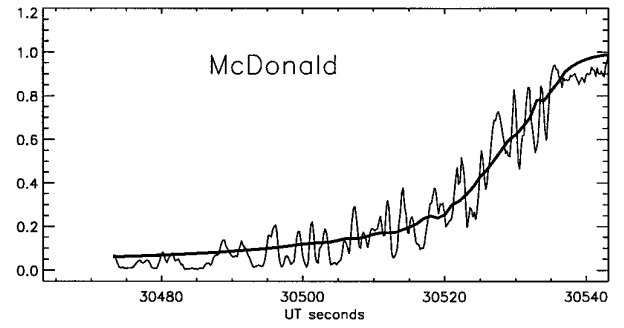
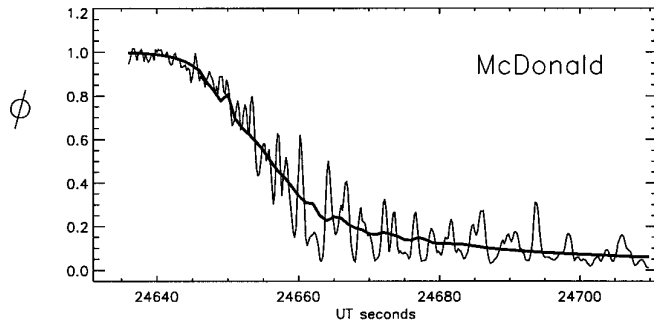
If the UVS data are not used to impose an outer boundary condition on the 28 Sgr inversions, then much greater uncertainties in the mesospheric temperature structure result. In the latter case, we cannot entirely rule out models of the type proposed by Yelle *et al.* for Jupiter’s meso-

sphere. Such a model with a temperature gradient (~ 1 K/km) at pressures ~ 0.5 μ bar is compatible with our stellar occultation data.

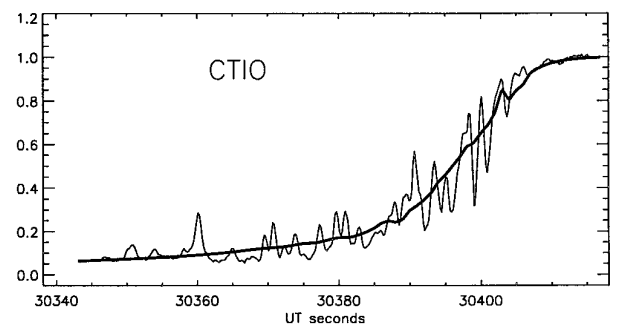
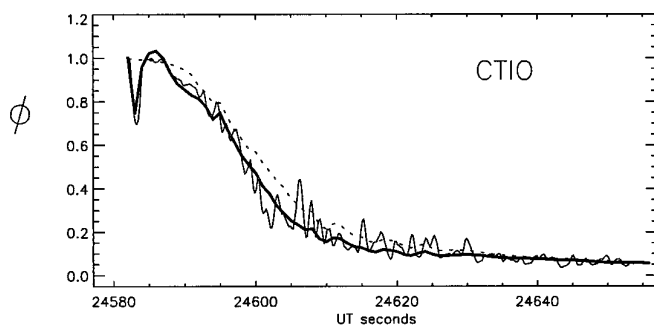
Within 20° of the equator, Saturn’s mesosphere shows an outward bulge of about one scale height with respect to level surfaces in the magnetic-field-stationary frame. This bulge is evidently supported by strong zonal winds moving at the same velocities (~ 450 m/sec) as zonal winds seen near 1 bar, much deeper in the atmosphere. Our result is not incompatible with the findings of Nicholson *et al.* (1995) and Conrath and Pirraglia (1983), who determined that at latitudes *greater* than 20° from the equator, zonal winds decay substantially with altitude. In particular, Nicholson *et al.* (1995) found indications from the 28 Sgr central flash data that oscillations in the midlatitude wind pattern decay in amplitude with height, but that the overall zonal wind pattern in these latitudes is still positive with a value of 40 m/s at the 2.5 mbar level (see Sec. 5.3 of Nicholson *et al.* 1995). Using Voyager infrared spectral measurements and the thermal wind equation, Conrath and Pirraglia found that temperatures varied by about 10 K on an isobaric surface at 150 mbar, over latitudes from -20° to $+20^\circ$, suggesting, according to the thermal wind equation, substantial decay of zonal winds with altitude within this latitude range. Our measurements of individual temperatures at various latitudes (Fig. 7) have error bars and scatter such that we cannot resolve temperature differences at the level reported by Conrath and Pirraglia. Note that Conrath and Pirraglia found a north–south temperature asymmetry within this latitude range of about 5 K, which we have averaged out in one of our models. Because we have averaged out any asymmetry, the actual altitude distortion in Saturn’s isopycnic surfaces might be slightly larger than that built into our baseline model. The alternate model fits the data about as well as the baseline model for Saturn’s shape. Based on the equatorial distortion which we measure, equatorial zonal winds with speeds of about 450 m/s must persist undiminished at $P \sim 1$ μ bar ($a \approx 61,000$ km).

Improved measurements of Saturn’s atmosphere for $a > 61,000$ km by means of a UV occultation experiment on board future Saturn spacecraft could lead to a better application of the constraints from the 28 Sgr data for the atmosphere in the interval $60,800 < a < 61,000$ km. But in the meantime, an isothermal model at $T = 140$ K (assuming $\mu = 2.135$) throughout this interval provides an excellent fit to the data.

As the lightcurves presented in this paper show, strong scintillations of the star appear in all records, and are the strongest source of error in determining atmospheric struc-



ESO 1m emission
not observed



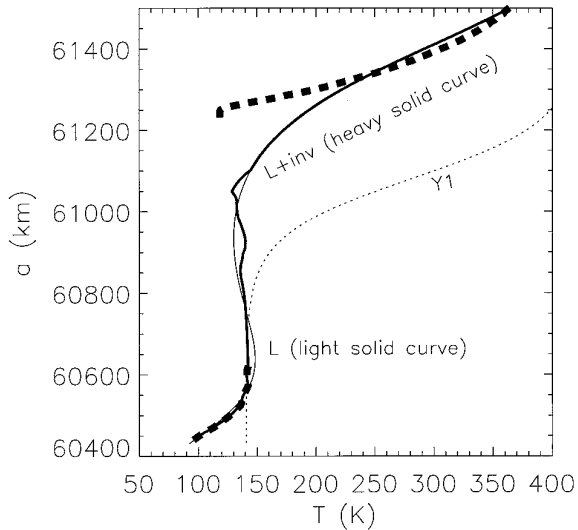


FIG. 16. A summary of models that fit the 28 Sgr data. As before, Heavy dashed curves are Voyager UVS (upper) and RSS (lower) data. Smooth light curve is the L model. Heavy solid curve is model L + inv. Dotted curve is model Y1.

ture. The statistics of these scintillations and their implications for the dynamics of Saturn's mesosphere remain to be investigated (as is also the case for the scintillations observed during the occultations of 28 Sgr by Titan). As discussed by French and Gierasch (1974), and subsequently by Yelle *et al.* (1996), the scintillations may be related to wave processes leading to the observed temperature distributions in the mesospheres of giant planets.

ACKNOWLEDGMENTS

This work has been supported by NASA Grants NAGW-1555, NAG5-4214, NAGW-1876, NAGW-1368, and NAG5-4214 and by NSF Grants AST-8715373 and AST-9322115. C. Porco and V. Haemmerle acknowledge support under NASA Grants NAGW-3411 and NAGW-1876. We thank Bruno Sicardy for assistance in preparing the ESO observations. We thank Phil Nicholson and another referee for helpful comments.

REFERENCES

- Baron, R. L., R. G. French, and J. L. Elliot 1989. The oblateness of Uranus at the 1- μ bar level. *Icarus* **78**, 119–130.
- Baum, W. A., and A. D. Code 1953. A photometric observation of the occultation of σ Arietis by Jupiter. *Astron. J.* **58**, 108–112.
- Bosh, A. S. 1994. *Stellar Occultation Studies of Saturn's Rings with the Hubble Space Telescope*. Ph.D. Thesis, Massachusetts Institute of Technology.
- Campbell, J. K., and J. Anderson 1989. Gravity field of the saturnian system from *Pioneer* and *Voyager* tracking data. *Astron. J.* **97**, 1485–1495.
- Conrath, B. J., and J. A. Pirraglia 1983. Thermal structure of Saturn from Voyager infrared measurements: Implications for atmospheric dynamics. *Icarus* **53**, 286–292.
- Elliot, J. L., L. H. Wasserman, J. Veverka, C. Sagan, and W. Liller 1974. The occultation of β Scorpii by Jupiter. II. The hydrogen–helium abundance in the jovian atmosphere. *Astrophys. J.* **190**, 719–729.
- French, R. G., J. L. Elliot, and P. Gierasch 1978. Analysis of stellar occultation data: Effects of photon noise and initial conditions. *Icarus* **33**, 186–202.
- French, R. G., and P. J. Gierasch 1974. Waves in the jovian upper atmosphere. *J. Atmos. Sci.* **31**, 1707–1712.
- French, R. G., P. D. Nicholson, M. L. Cooke, J. L. Elliot, K. Matthews, O. Perković, E. Tollestrup, P. Harvey, N. J. Chanover, M. A. Clark, E. W. Dunham, W. Forrest, J. Harrington, J. Pipher, A. Brahic, I. Grenier, F. Roques, and M. Arndt 1993. Geometry of the Saturn system from the 3 July 1989 occultation of 28 Sgr and Voyager observations. *Icarus* **103**, 163–214.
- Gautier, D., and T. Owen 1989. The composition of outer planet atmospheres. In *Origin and Evolution of Planetary and Satellite Atmospheres* (S. K. Atreya, J. B. Pollack, and M. S. Matthews, Eds.), pp. 487–512. Univ. of Arizona Press, Tucson.
- Harrington, J., M. L. Cooke, W. J. Forrest, J. L. Pipher, E. W. Dunham, and J. L. Elliot 1993. IRTF observations of the occultation of 28 Sgr by Saturn. *Icarus* **103**, 235–252.
- Hubbard, W. B., V. Haemmerle, C. C. Porco, G. H. Rieke, and M. J. Rieke 1995. The occultation of SAO 78505 by Jupiter. *Icarus* **113**, 103–109.
- Hubbard, W. B., C. C. Porco, D. M. Hunten, G. H. Rieke, M. J. Rieke, D. W. McCarthy, V. Haemmerle, R. Clark, E. P. Turtle, J. Haller, B. McLeod, L. A. Lebofsky, R. Marcialis, J. B. Holberg, R. Landau, L. Carrasco, J. Elias, M. W. Buie, S. E. Persson, T. Boroson, S. West, and D. J. Mink 1993a. The occultation of 28 Sgr by Saturn: Saturn pole position and astrometry. *Icarus* **103**, 215–234.
- Hubbard, W. B., B. Sicardy, D. M. Hunten, A. Brahic, C. Ferrari, D. Gautier, J. Lecacheux, E. Lellouch, F. Roques, J. E. Arlot, F. Colas, W. Thuillot, F. Sèvre, J. L. Vidal, C. Blanco, S. Cristaldi, C. Buil, A. Klotz, E. Thouvenot, H. J. Reitsema, N. Brosch, Y. Nevo, E. Carreira, F. Rossi, L. H. Wasserman, C. C. Porco, R. V. Yelle, B. Rizik, W. Beisker, M. Nezel, B. Riedel, H. Denzau, K. Zdanavicius, K. Cernis, M. Hoffmann, E. H. Geyer, R. W. Forrest, I. K. M. Nicolson, R. Miles, G. Appleby, F. M. Flasar, D. Toublanc, and G. Corugedo 1993b. The occultation of 28 Sgr by Titan. *Astron. Astrophys.* **269**, 541–563.
- Lindal, G. F., D. N. Sweetnam, and V. R. Eshleman 1985. The atmosphere of Saturn: An analysis of the Voyager radio occultation measurements. *Astron. J.* **90**, 1136–1146.
- Nicholson, P. D., C. A. McGhee, and R. G. French 1995. Saturn's central flash from the 3 July 1989 occultation of 28 Sgr. *Icarus* **113**, 57–83.
- Nicholson, P., and C. Porco 1988. A new constraint on Saturn's zonal gravity harmonics from Voyager observations of an eccentric ringlet. *J. Geophys. Res.* **93**, 10,209–10,224.
- B. Sicardy, A. Brahic, C. Ferrari, D. Gautier, J. Lecacheux, E. Lellouch, F. Roques, J. E. Arlot, F. Colas, W. Thuillot, F. Sèvre, J. L. Vidal, C. Blanco, S. Cristaldi, C. Buil, A. Klotz, and E. Thouvenot 1990. Probing Titan's atmosphere by stellar occultation. *Nature*, **343**, 350–353.
- Smith, G. R., D. E. Shemansky, J. B. Holberg, A. L. Broadfoot, B. R. Sandel, and J. C. McConnell 1983. Saturn's upper atmosphere from the Voyager 2 EUV solar and stellar occultations. *J. Geophys. Res.* **88**, 8667–8678.
- Tassoul, J.-L. 1978. *Theory of Rotating Stars*. Princeton Univ. Press, Princeton, NJ.
- Wasserman, L. H., and J. Veverka 1973. On the reduction of occultation light curves. *Icarus* **20**, 322–345.
- Yelle, R. V., L. A. Young, R. V. Vervack, Jr., R. Young, L. Pfister, and B. R. Sandel 1996. Structure of Jupiter's upper atmosphere: Predictions for Galileo. *J. Geophys. Res.* **101**, 2149–2161.